COMPARISON OF MODELING METHODS FOR POWER CYCLE COMPONENTS USING SUPERCRITICAL CARBON DIOXIDE AS THE OPERATING FLUID

by

JOSHUA MICHAEL SCHMITT
Bachelor of Science in Mechanical Engineering
University of Florida, 2010

A thesis submitted in partial fulfillment of the requirements
for the degree of Master of Science in Mechanical Engineering
in the Department of Mechanical and Aerospace Engineering
in the College of Engineering and Computer Science
at the University of Central Florida
Orlando, Florida

Summer Term
2015

Major Professor: Jayanta Kapat

ABSTRACT

Supercritical carbon dioxide as a working fluid in a Brayton power cycle has benefits but also faces unique challenges in implementation. With carbon dioxide, turbomachinery is much more compact and potentially more cost effective. The primary impediments to cycle component performance are the high pressures required to bring the fluid to a supercritical state and the wildly varying fluid properties near the critical point. Simple design models are often used as a quick starting point for modern turbomachinery and heat exchanger design. These models are reasonably accurate for design estimate, but often assume constant properties. Since supercritical carbon dioxide varies not only in temperature, but also in pressure, the models must be evaluated for accuracy. Two key factors in cycle design, aerodynamics and heat transfer, are investigated through the modeling of the performance of the first stage of the turbo-expander and the recuperative heat exchangers. Lookup tables that define the change in fluid properties relative to changes in pressure and temperature are input into the fluid dynamics software. The results of the design models are evaluated against each other. The simpler models and the fluid dynamics simulations are found to have acceptable agreement. Improvements to the simple models are suggested.

ACKNOWLEDGMENTS

This body of work would not be possible without the support of the Laboratory for Cycle Innovation and Optimization as part of the Center for Advanced Turbomachinery and Energy Research at the University of Central Florida. The leadership and experience of David Amos was invaluable to the completion of this work, along with the support and insight of past and present members of the Cycle Innovation group, including: Mahmood Mohagheghi, Rachel Willis, Ravikiran Kattoju, Adam Jensen, and others.

I would like to thank the other students of the CATER labs, who have often provided advice and support leading up to the completion of this thesis. They include: Justin Hodges, Constantine Wolski, Sergio Arias Quintero, Stephen Stafstrom, Brandon Ealy, Cassandra Carpenter, Chris Vergos, Tyler Voet, Jahed Hossain, and others.

Nicole, my fiancée, has been a source of strength and an endless fountain of love. Her unfailing commitment has kept me afloat, and this work would not have been possible without her. I would also like to dedicate this work to my parents and all the love, time, money, and effort they have invested in me; it is finally paying off. My brother and sister have been amazing through all this, providing help when I needed it. I would also like to thank my church, True Freedom Fellowship, and the emotional and mental support they provide every week.

Last, but certainly not least, I want to deeply thank Dr. Jay Kapat for paving the way for this thesis. His guidance and knowledge were integral to the writing of this thesis. I deeply appreciate all the work he has done on my behalf to provide me with so many academic and professional opportunities. Thank you.

TABLE OF CONTENTS

LIST OF FIGURES

LIST OF TABLES

NOMENCLATURE

c	Airfoil chord, cm
C	Flow absolute velocity, m/s
c_p	Specific heat capacity, J/kg-K
C_z	Axial flow absolute velocity, m/s
D_{hyd}	Hydraulic diameter, m
E	Modulus of elasticity, GPa
eff	Exchanger effectiveness
f	Darcy friction factor
h	Enthalpy, kJ/kg
H	Annular height, cm
h_o	Convective heat transfer coefficient, W/m^2-K
k	Thermal conductivity, W/m-K
$LMTD$	Log mean temperature difference, K
$\dot{m}$	Mass flow rate, kg/s
N_w	Number of walls of heat transfer
Nu	Nusselt number
p	Airfoil pitch, cm
P	Pressure, Pa
Pr	Prandtl number
$\dot{Q}$	Heat transfer, W
R	Thermal resistance, m^2-K/W
r_m	Mean-line radius, cm
R_o	Row reaction
Re	Reynolds number
s	Square channel side, m
t	Exchanger internal wall thickness, m
T	Temperature, K
U	Mean-line wheel speed, m/s
U_o	Convective heat transfer coefficient, W/m^2-K
w	Airfoil axial width, cm
W	Flow relative velocity, m/s

Greek

α_t	Coefficient of thermal expansion, μm/μm-K
α	Flow absolute angle, degrees (°)
β	Flow relative angle, degrees (°)
ΔP	Change in pressure across control volume, Pa
ΔT	Change in temperature across control volume, K
Δx	Length of control volume, m
ε	Cascade turning angle

ε_o	Absolute roughness
η_{TS}	Total-to-static efficiency, %
η_{TT}	Total-to-total efficiency, %
ζ	Loss coefficient
μ	Dynamic viscosity, kg/s-m
ρ	Density, kg/m^3
σ_b	Bending stress, MPa
φ	Flow coefficient
ψ	Work coefficient
Ψ_T	Zweifel parameter
ω	Angular velocity, rad/s

Subscript

1,2,3	*Stage* locations: before stator, between stator and rotor, after rotor
avg	Average value
cond	Conduction
conv	Convection
c	Cold
f	Fluid
h	Hot
i	Row number in a 2-D table
isen	Isentropic
j	Column number in a 2-D table
lat	Lateral
mat	Heat exchanger material
n	Control volume number
R	Rotating airfoil
S	Stationary airfoil

Acronyms

CFD	Computational Fluid Dynamics
HTR	High Temperature Recuperator
LTR	Low Temperature Recuperator
RRC	Recuperated Recompression Cycle
SCO_2	Supercritical Carbon Dioxide
SST	Menter's Shear Stress Transport turbulence model

1 INTRODUCTION

Power cycles using supercritical carbon dioxide (SCO_2) as the primary working fluid have a strong potential for widespread adoption in the power generation industry. Due to the high density of SCO_2, the turbomachinery and heat exchange components experience a dramatic reduction in scale versus air and steam based cycles. The concept of a SCO_2 power cycle has existed since 1967; however, practical implementations have only recently gained momentum with advancements in advanced manufacturing techniques, compact heat exchanger design, and turbomachinery design (Dostal, 2004). With the increasing interest from academic and commercial entities, the United States Department of Energy has awarded funding to companies and universities to develop these cycles on the laboratory scale.

The cycle has already been developed for commercial waste heat recovery applications for power outputs as high as 400 kW. If scaled up, the SCO_2 system can perform as a bottoming cycle to a gas turbine in a combined cycle power plant. At this scale, the plant footprint can be two-thirds the size of a combined cycle plant utilizing steam. The overall compactness of a SCO_2 cycle can reduce capital and operational costs, resulting into a reduced levelized cost of electricity by about 10 to 20 percent (Persichilli, Kacludis, Zdankiewicz, & Held, 2012)

The SCO_2 cycle, operating in a closed loop, is not limited to waste heat recovery, but can generate power as the primary cycle through energy added from compact heat exchangers. The Massachusetts Institute of Technology (Dostal, 2004), Knolls Atomic Power Laboratory, and Bettis Atomic Power Laboratory (Kimball & Clementoni, 2012) conduct research into the application of this cycle to a nuclear power source. The diminished size of the turbomachinery is attractive to developers of nuclear powered naval vessels, where space is limited.

Concentrating solar power is another source of heat energy that is well-suited to SCO_2 power cycles. A study conducted by the National Renewable Energy Laboratory published that simple recuperated SCO_2 cycles in a modular solar power tower can achieve 44% efficiency. The more advanced recuperated recompression cycle (RRC), which is the cycle chosen in this thesis, can reach 51% efficiency. The maximum cycle temperature is limited by solar availability and technologies. But even with low temperatures SCO_2 cycles can achieve these efficiencies, whereas simple steam cycles perform less efficiently (Turchi, Ma, & Dyreby, 2012).

Sandia National Laboratories and Barber-Nichols Inc. have published on their joint test loop with a turbine inlet temperature of 811 K that can achieve 780kW output, with hopes to reach 1MW (Pasch, Conboy, Fleming, & Rochau, 2012). As laboratories increase the capacity of their SCO_2 cycles, they begin to approach a size that is comparable to modern, commercial power systems.

The goal of this study is to expand the scientific understanding of SCO_2 power cycle design and modeling towards large, commercially viable power plants. With this in mind, a 100MW cycle output is targeted with a 1350 K turbine inlet temperature. Power generation blocks using gas turbines can easily reach these goals. The SCO_2 design must be able to produce a competitively sized system with a lower cost of electricity in order to be adopted by industry. Because modeling SCO_2 property change with its temperature and pressure dependencies can be difficult, the design methods of industrially sized system components should be scrutinized and assessed for validity.

2 LITERATURE REVIEW

A wealth of knowledge exists about the component design, modeling, and performance of conventional steam and gas turbines. The same techniques are being applied to the design of SCO_2 power cycle components. However, supercritical fluid does not behave like an ideal gas, especially near the critical point. Thus, the design experience of conventional power cycles needs to be understood and modified to better describe the behavior of SCO_2 as a working fluid. First, accepted design methods and modeling should be examined, and then the behavior of SCO_2 must be integrated into the modeling techniques.

2.1 Key Cycle Component Design and Modeling Techniques

Turbo-expanders are the primary driver of a power cycle. In an axial expander, stationary and rotating airfoils alternate in a cascade, and the expanding fluid provides work to the rotating airfoils, turning a shaft. The basis for modern axial turbomachinery design comes from early aerodynamic studies by Horlock (1966), Dixon (1975), Soderberg (1949), Ainley & Mathieson (1957), and Zweifel (1946). These early publications created one-dimensional and three-dimensional design approaches that can effectively and quickly model the performance of an axial turbine.

Many studies have since validated and expanded upon these early modeling methods. An experimental validation of profile loss models have found that these models still predict performance to between 1% to 2% improved at the design point (Jouybar, Eftari, Kaliji, Ghadak, & Rad, 2013). The pitch selection criteria were also evaluated experimentally in air and the

results were between 5% to 6% lower than the models predicted (Wei, 2000). Thus, the simpler modeling is in good agreement with experimental results for air, but these models must be assessed for SCO_2. Wei notes that when the turbomachinery operates away from the design point, the cost to performance could be as high as 20%. Therefore, accurate modeling is essential for finding the correct design point and maximizing turbo-expander efficiency.

Current experimentation into aerodynamic turbomachinery design focuses on radial impeller compressors. Initial test loops of SCO_2 cycles have experimented primarily with radial compressors, creating detailed maps of compressor performance (Wright, Radel, Vernon, Rochau, & Pickard, 2010). This study the radial compressor was able to perform as high as 67% efficiency despite the small, laboratory scale incurring greater rotor tip losses. The recompressor efficiency was more impressive, reaching as high as 86% in the performance map (Pasch, Conboy, Fleming, & Rochau, 2012). The design philosophy for this loop uses performance charts and specific speed and diameter (Fuller, Preuss, & Noall, 2012), using Balje's (1981) method as a starting point for design. This is a simpler approach that uses non-dimensional factors mapped to a performance map. A similar approach will be applied to the axial turbine modeled in this thesis, using work coefficient and flow coefficient to model the performance of an axial turbine stage.

Heat exchangers are a key component to effective SCO_2 power cycles. New techniques of manufacturing compact heat exchangers which are formed through diffusion bonding provide a compact and strong solution. Because the SCO_2 operates with a high pressure differential between channels, the stresses must be mitigated. With a standard shell and tube exchanger, this would require thicker vessel and pipe walls, which is detrimental to heat transfer. Heatric

provided a detailed analysis of stress and the diffusion bonding process of their printed circuit heat exchanger (Southall, 2009). The diffusion-bonded layers behave as one single component free of joints, which would amplify stresses.

The sheets of a diffusion-bonded printed circuit heat exchanger are often designed with a cross-flow configuration stacked with alternating layers of hot and cold fluid flow. An exchanger with small channels, often a millimeter wide, are appealing for the high pressures of SCO_2, because the mass flow through each channel is reduced and the stress more easily distributed allowing for thinner walls separating hot and cold fluid. In order to maximize the area of heat exchange, Carman (2002) suggests designs of a counter-flow exchanger with alternating triangular and square "checkerboard" cross sections for use in an air cycle. Such a square channel exchanger is reported to have an effectiveness of 96.4% and a pressure loss of 3%. Carman also provides a heat transfer model and stress analysis that is the basis for the heat exchanger design in this thesis.

2.2 SCO_2 Property Behavior and Computational Evaluation

The properties of SCO_2 can change dramatically, especially at the lower temperatures and pressures in the cycle. The National Institute of Standards and Technology publishes a reference database of fluid properties, including carbon dioxide. Known as REFPROP (Lemmon, Huber, & McLinden, 2013), it is used as a lookup database for supercritical fluid properties. This is the standard used in this thesis for evaluating SCO_2 property behavior. The validity of heat transfer correlations of the properties taken from this database is experimentally evaluated by Liao &

Zhao (2002). They found that measured Nusselt numbers had a mean relative error of 9.8% from what is predicted by REFPROP with a measurement uncertainty of about 4%.

Computational fluid dynamics (CFD) modeling of a fluid with properties that vary in temperature and pressure can be difficult to achieve. With emphasis on nuclear reactors, Chataraju (2011) analyzed water at the critical point with the CFD software Star-CCM+. That work validated the ability of Star-CCM+ to model supercritical fluid conditions with experimental results. Chataraju developed a plugin to the software that can read water property tables dependent on temperature and pressure. Because of this effort, the developer of the software, CD-Adapco, integrated a two-dimensional table lookup system into their software package. This lookup method in Star-CCM+ is used to model SCO_2 as part of this thesis.

Zhou's thesis (2014) continues Chataraju's work and models both supercritical water and supercritical carbon dioxide through CFD. Through this work, Zhou suggests that the shear-stress transport (SST) k-ω model is more stable, robust and easier to converge. Wang (2014) correlated a CFD simulation of SCO_2 to experimental data of heat transfer in helically coiled tubes. The turbulence model recommended from that study was the SST model, which followed experimental heat transfer coefficients and wall temperatures closely, only deviating by a maximum of 10%. Following these recommendations, the SST model is used in this thesis for describing turbulence behavior in CFD.

3 CARBON DIOXIDE PROPERTY VARIATIONS

Carbon dioxide transitions into a critical state above the temperature of 304.25 K and at pressures beyond 7.38 MPa. Near this transition point, the physical characteristics of the fluid undergo dramatic changes. Quantitative experimentation confirms the behavior of carbon dioxide properties (Liao & Zhao, 2002) to the REFPROP (Lemmon, Huber, & McLinden, 2013) database and demonstrates the improvements that can enhance heat transfer. Using the same database, various fluid properties are graphed in Figure 3-1 near the critical point and well into the critical region.

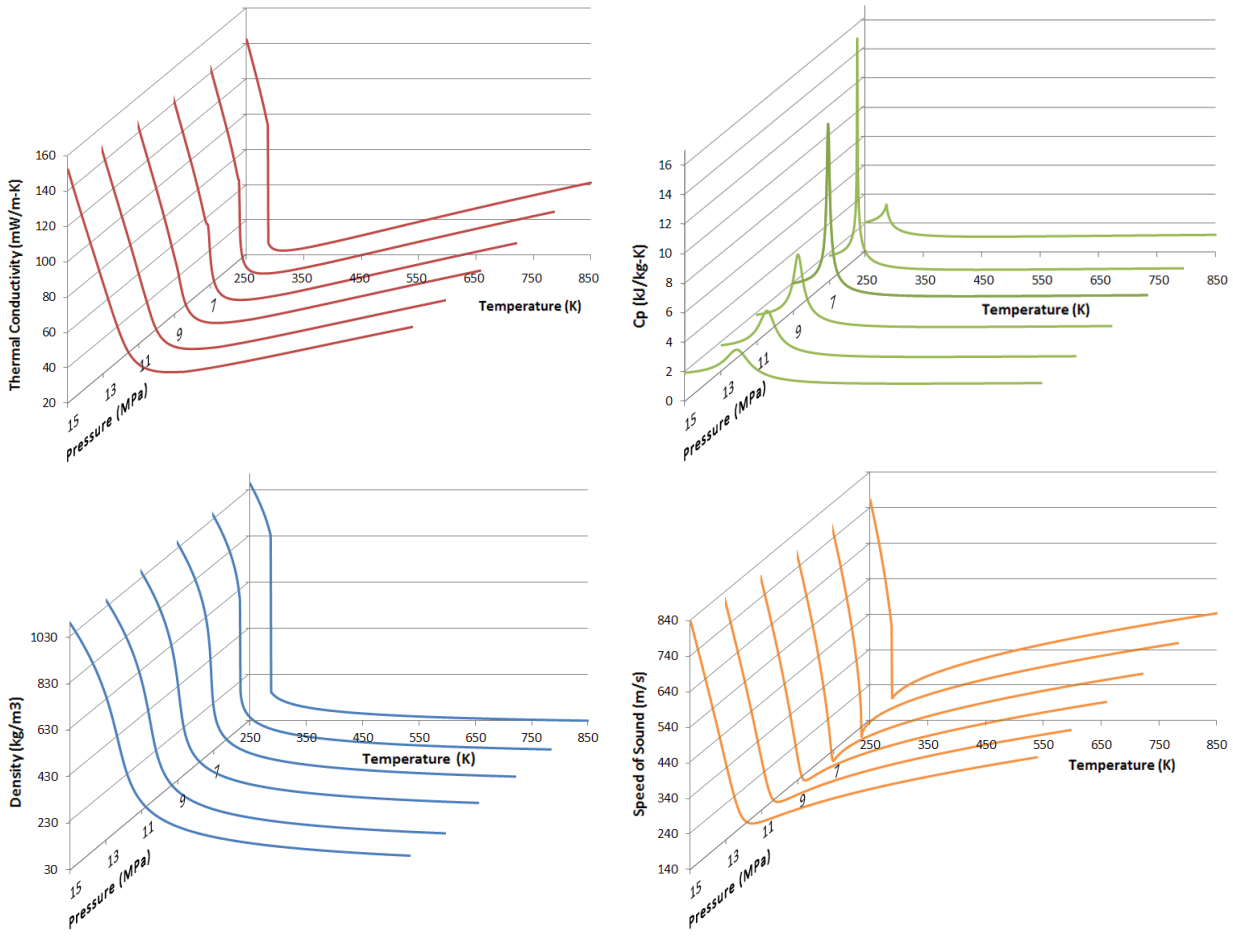

Figure 3-1: Variation of specific heat, thermal conductivity, density, and the speed of sound

According to Figure 3-1, transitioning from a liquid to a supercritical fluid provides the most dramatic change in behavior. If the temperature is much hotter than the critical point, but the pressure drops below the critical point, then the fluid transitions to a gas. The properties behave similar to that of a typical gas, depending only on temperature and not varying much with changes in pressure. Near the critical point all of these property values are a function of both temperature and pressure. However, even at pressures well above the critical point, the transition in temperature from liquid to supercritical fluid represents a dramatic change in every chart in Figure 3-1. Because of this, cycles have been suggested that operate into the liquid phase of carbon dioxide, similar to the way a steam Rankine cycle takes advantage of the phase change of water. However, research into a compression loop describes the challenges of operating a cycle near the critical point (Wright, Radel, Vernon, Rochau, & Pickard, 2010), indicating that a successful cycle may want to have its lowest point in the supercritical region and not experience a phase change.

One key property where the fluctuation near the critical point can provide an advantage is the thermal conductivity. As displayed in the top-left graph of Figure 3-1, the thermal conductivity of the fluid dips as the temperature approaches the critical temperature, and then rises again near the critical point. The heat transfer coefficient would decrease and then increase moving away from the critical point in temperature. Near the critical point, pressure variation plays a greater role, improving thermal conductivity for higher pressures.

The specific heat at constant pressure (c_p) or the ratio of specific heats (c_p/c_v) is used in axial turbine design. The design approach assumes a constant specific heat across an airfoil cascade. However, as shown in the top-right chart in Figure 3-1, the specific heat jumps wildly

when the temperature nears the critical temperature. The change in specific heat is the most dramatic near the critical pressure, but the specific heat still does not remain constant near the critical point for high pressures with a temperature near the critical point. This indicates that the design of the compressor turbine, which is at the lower temperature side of the cycle, is greatly impacted by this fluid behavior. The turbo-expander, however, will usually operate at a temperature where the fluid behaves like a compressible gas, allowing for more traditional design methods.

Another key factor in turbomachinery design is the density and the speed of sound, seen in Figure 3-1 on the bottom-left and the bottom-right, respectively. The density is very high on the compressor side of the cycle, but much lower in the turbo-expander. High fluid density results in a smaller compressor annular area, which forces the overall diameter of the turbomachinery to reduce in size dramatically. While the cost of manufacturing the machinery decreases, other design challenges arise such as rotor loading, airfoil performance, and sealing. Furthermore, the speed of sound drops dramatically near the critical point, making it very easy for fluid to reach supersonic speeds in areas of high compressibility. Supersonic flow is bad for turbomachinery design because it can create potentially harmful shocks and losses that highly degrade performance.

Because of all these challenges, robust design tools must be developed to account for the behavior of SCO_2. Simple modeling methods are available that read fluid properties from the REFPROP database directly. Through add-ins available for Matlab and Microsoft Excel, design methods that assume constant properties can be updated with new property values. CFD packages, such as a Star-CCM+, are Reynolds-averaged Navier-Stokes equation solvers. These

also require robust input methods so that the fluid properties are properly updated with temperature and pressure. Chatharaju (2011) proposes a two-dimensional table lookup method, which is now implemented by the developers of Star-CCM+. At the beginning of this study, viscosity and conductivity were implemented for one-dimensional tables that are dependent on temperature only. Per the request of the author of this thesis, the two-dimensional lookup method was made available for all properties in the Star-CCM+ software package.

$$f(T,P) = f_{i,j} + \left(f_{i+1,j} - f_{i,j}\right)\frac{T - T_i}{T_{i+1} - T_i} + \left(f_{i,j+1} - f_{i,j}\right)\frac{P - P_j}{P_{j+1} - P_j} + \left(f_{i+1,j+1} - f_{i+1,j} - f_{i,j+1} + f_{i,j}\right)\frac{T - T_i}{T_{i+1} - T_i}\frac{P - P_j}{P_{j+1} - P_j} \quad \textbf{(3-1)}$$

The table lookup uses a multi-variable bilinear interpolation method to find properties for a given temperature and pressure, shown in Equation 3-1. The property needing to be interpolated is between the temperatures in row i and i+1, and between the pressures in column j and j+1. A code is developed that generates random values of temperature and pressure and compares the interpolated result from the table to the property output from REFPROP. Using this approach, it is determined that the interpolation becomes more inaccurate the closer the temperature and pressure are to the critical point. This is a logical result because, as seen in Figure 3-1, the properties undergo large changes in slope near the critical point. Decreasing the change in temperature or the change in pressure per column or per row improves the accuracy of interpolation, but also increases size of the table. Larger tables require more the time per iteration of the CFD solution. The interpolation error code is implemented to find the appropriate table spacing, setting a goal of less than 0.5% deviation of the interpolated number from the database value, while making tables as small as possible.

4 CYCLE OPTIMIZATION

The design of a SCO_2 power cycle begins with an optimized cycle analysis. The cycle design follows the method outlined by Mohagheghi and Kapat (2013). The simple, recuperated cycle is efficient for configurations with low pressure ratios, like most SCO_2 power cycles. The optimization code uses a genetic algorithm to solve for the cycle balance of variations on the simple recuperated cycle. Cycles with combinations of recompression, reheat, and intercooling are all set up within the code. The recuperated recompression cycle (RRC) is chosen because of the significant improvement over the simple cycle. The RRC achieves these improvements while keeping the cycle components required to a manageable level. More complex the cycles increase the cost and maintenance concerns. Since the goal of this paper is to design a cycle sized for commercial power generation, the RRC provides a good balance between cost and efficiency.

Table 4-1: Key cycle input parameters

Max. Cycle Temp. (K)	Min. Cycle Temp. (K)	Max. Pressure (MPa)	Min. Net Power Out (MW)	Pinch Point Diff. (K)
1350	320	24	100	10

The cycle balance optimization uses key input parameters, highlighted in Table 4-1, to find the best cycle design. The maximum and minimum cycle temperatures are at the discretion of the designer. The maximum temperature is the hottest temperature deemed achievable in the turbo-expander. The chosen temperature, 1350 K, is within the capability of a modern gas turbine. The airfoils might need simple cooling channels to ensure that the metal does not reach temperatures above its material limit. The minimum temperature affects the compressor design. The closer the temperature is to the critical point, it is harder to model the fluctuating fluid

properties. However, the lower that temperature is, the better the cycle efficiency. A minimum temperature of 320 K is chosen to ensure that the main compressor can perform safely distant from the critical point. The minimum pressure is varied by the code, because the optimum value is not necessarily the lowest possible value (Mohagheghi & Kapat, 2013).

A minimum net power output of the cycle of 100 MW is specified to make this design feasible on a commercial scale. The maximum allowable pressure in the cycle is decided based on what pressures are achieved in modern ultra-supercritical steam turbines. The pinch point temperature of all the heat exchangers often decides the effectiveness of the heat transfer of these components. Thus the pinch point temperature is set to 10 K, the minimum value recommended by Mohagheghi and Kapat (2013). Each heat exchanger is assumed to transfer all available heat energy from the hot fluid to the cold fluid. The main compressor is selected to be a radial impeller with an estimated isentropic efficiency of 75%. The recompressor, chosen to be axial, is expected to achieve 80% isentropic efficiency. The design of these components, supported by accurate modeling, must achieve these target performances for the cycle to operate successfully.

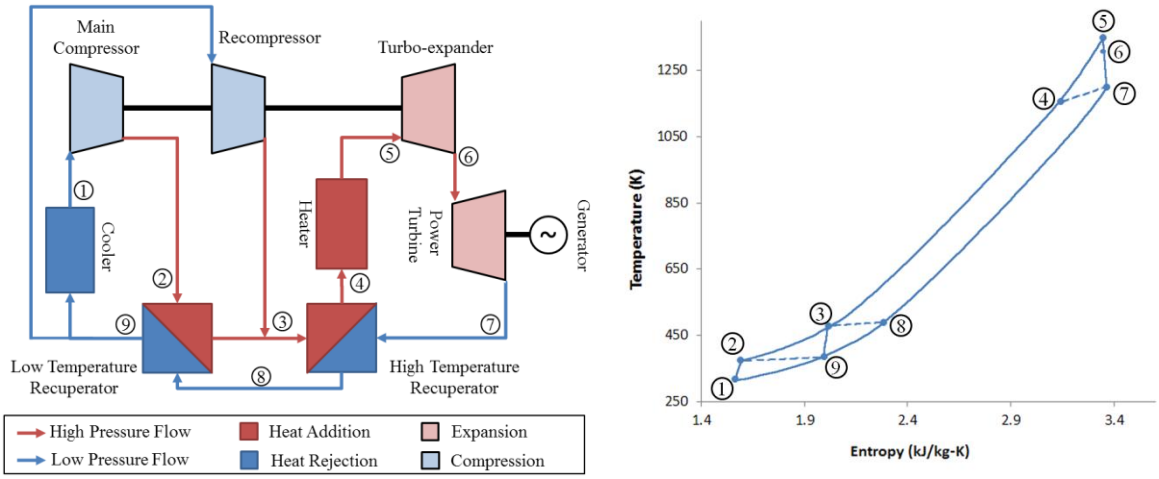

Figure 4-1: Optimized cycle block diagram and temperature vs entropy plot

The RRC component block diagram is shown on the left in Figure 4-1. The turbo-expander powers the two compressors directly while the power turbine connects to the generator on a separate shaft. This configuration was chosen so that the compressors and the turbo-expander could operate at high rotational speeds. The power turbine attached to the generator must spin at 3600 RPM to facilitate a connection to the grid. However, this relatively low speed would result in very short airfoils and passages in the compressors and turbo-expander, increasing losses.

The heat of the fluid leaving the power turbine is added into the cycle before the heater using a high temperature recuperator (HTR). The low temperature recuperator (LTR) provides energy needed to raise the temperature of the fluid at the discharge of the main compressor to the same state as the discharge of the recompressor. The pressure drop through these components is approximated and must be matched or improved upon in the design. The flow splits between the main compressor and a recompressor after heat is rejected from the LTR. Also in Figure 4-1 is the temperature vs entropy cycle diagram. This represents the fluid changes as it travels through the different components of the power cycle.

Table 4-2: Optimized cycle state points

State Point	Temperature (K)	Pressure (kPa)	Enthalpy (kJ/kg)	Density (kg/m3)
1	320.0	9641.2	376.9	394.3
2	376.7	24000.0	415.6	554.0
3	480.1	23880.0	596.0	303.3
4	1158.7	23760.6	1461.2	102.6
5	1350.0	23523.0	1713.0	87.3
6	1310.1	18984.0	1659.7	56.3
7	1201.6	9835.4	1518.2	42.3
8	490.1	9786.5	652.9	113.6
9	386.7	9737.8	525.7	167.7

The state points of the cycle are shown in Table 4-2. The state point numbers correspond to the fluid before and after various components in the cycle. Figure 4-1 labels these points in both the block diagram and the temperature vs entropy chart. According to the optimization code and given the initial design limits to the RRC configuration, this cycle is the most efficient cycle possible. Some other key results of this optimization are shown in Table 4-3.

Table 4-3: RRC optimized cycle performance parameters

Cycle Efficiency	Total Cycle Mass Flow	Compressor Inlet Pressure	Percent Main Compressor Mass Flow	Net Power Out	HTR Heat Load	LTR Heat Load
58.3 %	714.9 kg/s	9.641 MPa	70.6%	104.97 MW	618.6 MW	90.96 MW

The results show a competitively efficient cycle at 58.3%. The compressor inlet pressure is sufficiently distant from the critical point that the turbomachinery is not likely to be affected by the risks mentioned in the previous chapter. For the main compressor, 70.6% is found to be the optimal percentage of the total mass flow that is pressurized by the radial impeller. A higher flow rate places the larger work requirement on the less efficient main compressor. This results in a higher work load on the turbo-expander. The power turbine is able to provide above 100 MW of power, exceeding the minimum requirement. The heat load on both recuperators is very large, especially the HTR. This implies the accurate modeling of these heat exchangers is required, because they have a significant impact on the overall efficiency and cycle performance

5 AERODYNAMICS: AXIAL TURBOMACHINERY MODELING

As mentioned in chapter 4, the cycle has a twin shaft where the main compressor and the recompressor are connected to a turbo-expander. Thus, the performance of the turbo-expander is important to the successful operation of the cycle. The first stage, a stationary cascade followed by a rotating cascade of airfoils, is selected for analysis. The fluid is at its hottest point, far from the critical point, so the variation in thermodynamic properties is dependent on temperature, but not on pressure. However, the fluid travels at high enough speeds that it can be considered compressible, so the pressure variation in density and the speed of sound are a factor.

5.1 Turbo-expander First Stage Airfoils

The approach to designing and estimating the behavior of an axial turbine is sourced from Horlock (1966), Dixon (1975), and Ainley and Mathieson (1957). These works describe methods for predicting losses in a series of airfoil cascades. First, the cycle conditions at the turbo-expander inlet, state point 5, are taken from Table 4-2. Since the compressors and the turbo-expander are connected on the same shaft, the optimum operating speed must be an acceptable speed for all three turbomachines. Since the power turbine is decoupled from the shaft connecting the other three turbines, the turbo-expander can operate at a rotation rate higher than 3600 RPM. Considering the design implications to all attached components, a rotation speed of 8700 RPM is selected.

$$U = r_m \omega \tag{5-1}$$

The mean wheel speed, or the linear velocity at the rotating airfoil's mid-span point, is selected as a design limit. The wheel speed must be low enough so that the flow is not forced into supersonic velocities. The required radius to the mean-line is calculated using Equation 5-1 where the rotation speed is in radians per second. The stage performance depends on two dimensionless parameters: the flow coefficient, shown in Equation 5-2 and the stage loading coefficient, shown in Equation 5-3.

$$\varphi = \frac{C_z}{U} \tag{5-2}$$

$$\psi = \frac{\Delta h}{U^2} \tag{5-3}$$

$$\psi = \sqrt{1 + 4\varphi^2} \tag{5-4}$$

The turbine is designed to have a constant axial flow, so the flow coefficient remains constant in the turbo-expander. The work provided by a stage, as indicated by the loading coefficient must meet the work requirement of the two compressors. After calculating the work of the two compressors, the enthalpy change requirement of the turbo-expander is found to be 48.0 kJ/kg. This requirement is divided by the number of stages in the turbo-expander so that the per-stage loading is known. The loading coefficient is calculated using Equation 5-3. According to Horlock (1966), the maximum possible total-to-static efficiency of a stage follows the relationship in Equation 5-4. From this relationship, the optimum loading coefficient is calculated. From Equation 5-2 the axial velocity required to meet this optimum efficiency is determined.

$$H = \frac{\dot{m}}{2\pi r_m \rho C_z} \tag{5-5}$$

Once the axial velocity is found, the annular height of the turbo-expander is calculated using the relationship in Equation 5-5. This design process is iterated until an efficient design is characterized.

Table 5-1: First stage design parameters

Mean Wheel Speed (m/s)	Rotation Speed (RPM)	φ	ψ	Mass Flow Rate (kg/s)	C_z (m/s)	Height (cm)	Mean Radius (cm)
182.88	8700	0.529	1.456	714.9	96.813	6.71	20.07

The results of the optimum axial turbine design are found in Table 5-1. The design process reveals that one stage should be sufficient for powering the compressors. With a flow coefficient of 0.529 and a work coefficient of 1.456, the turbo-expander provides 48.7 kJ/kg of enthalpy change, which leaves 104.4 MW of available power for the power turbine. According to Horlock (1966), this stage design should perform above 90% for a 0.5 reaction stage design.

$$\tan\beta_2 = \frac{1}{2\varphi}(\psi - 2R_o) \quad \textbf{(5-6)}$$

With the stage loading and flow coefficients known, the stage reaction is optimized. For an initial point of comparison, the reaction is set to be 0.5 and then plugged into Equation 5-6, allowing one of the flow angles, β_2, to be solved. From this angle, all absolute and relative velocities with their corresponding angles are determined. According to Soderberg (1949), the amount of turning flow must go through represents the most significant loss.

$$\zeta = 0.04\left[1 + 1.5\left(\frac{\varepsilon}{100}\right)^2\right] \quad \textbf{(5-7)}$$

The absolute angles, for the stationary airfoil, and the relative angles, for the rotating airfoil, are summed to find the total turning of the flow. This is brought into the correlation in

Equation 5-7. The loss of each airfoil cascade, the criteria for overall performance, is used to find the overall stage efficiency with Equation 5-8 and Equation 5-9. The 0.5 reaction design does not perform up to the standards of performance, so the reaction was adjusted until the efficiency is satisfactory. Thus the aerodynamic design of the cascade experienced several iterations in design.

$$\eta_{TT} = \left[1 + \varphi \frac{{\zeta_R}/{\cos^2 \beta_3} + {\zeta_S}/{\cos^2 \alpha_2}}{2 \tan \alpha_2}\right]^{-1} \quad \textbf{(5-8)}$$

$$\eta_{TS} = \left[1 + \varphi \frac{{\zeta_R}/{\cos^2 \beta_3} + {\zeta_S}/{\cos^2 \alpha_2} + 1}{2 \tan \alpha_2}\right]^{-1} \quad \textbf{(5-9)}$$

The final reaction resulted in a larger angle value for α_2 and a stage reaction less than 0.5 at the mean-line. A visual example of how the airfoils interact with each other is demonstrated in Figure 5-1. The flow enters the turbo-expander axially and is turned by the stationary row. One of the key considerations of designing a mean-line airfoil profile is the angle of incidence as the flow comes into contact with each airfoil. The curve of the airfoil must match the flow direction as closely as possible or further losses occur as the incidence angle deviates from design. The stationary airfoil follows absolute angles and the rotating airfoil follows relative angles.

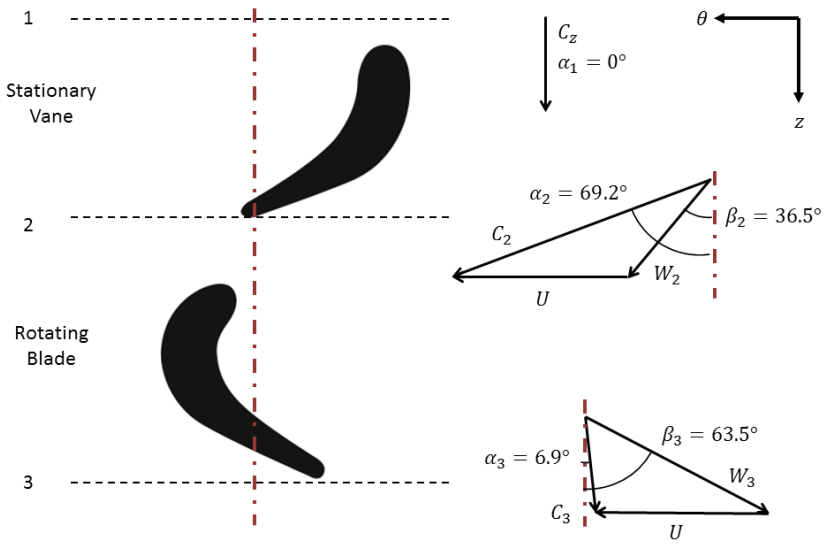

Figure 5-1: Turbine first stage one-dimensional design velocity triangles

With a properly performing mean-line profile, the three-dimensional nature of the airfoils is designed. The annular area increases with a constant, linear profile. The mean-line radius remains fixed throughout the turbo-expander. Thus, the increase in rotating airfoil height across the stage is known from the annular height at the beginning and the end of the stage.

The process for finding velocity profiles at the hub and casing follows the same procedure as the mean-line design with one further criterion: radial equilibrium must be satisfied. In order to model this, a free vortex condition is assumed. Under this assumption, the product of the absolute tangential velocity and the radius must be equal across an airfoil. Since the tangential velocity is known at the mean-line, and the radii of the hub and the tip are also known, the absolute tangential velocity is found. From this information the velocity triangles are found for the hub and the casing. The result of this procedure is documented in Table 5-2. These are the results that are compared to the CFD results.

Table 5-2: Results of the one-dimensional airfoil design

	Hub	Mean	Casing
φ	0.636	0.529	0.454
α_2(°)	72.42	69.18	66.07
α_3(°)	8.26	6.90	5.92
β_2(°)	57.74	36.54	2.82
β_3(°)	59.80	63.55	66.57
ε_S(°)	72.42	69.18	66.07
ε_R(°)	117.54	100.09	69.40
R	0.0427	0.336	0.512
ζ_S	0.0715	0.0687	0.0662
ζ_R	0.123	0.100	0.0689
η_{TS}(%)	81.4	82.9	84.4
η_{TT}(%)	88.7	90.5	92.2

The studies of Ainley and Mathieson (1957) suggest that an aspect ratio of 1.0 is ideal for the first stage stationary airfoils. According to that study, an increase in the aspect ratio to 1.4 decreases the losses. For this aspect ratio, the chord of the rotating airfoil reduces, and the rotor height increases. The shape of the airfoils at the hub and casing are known and the chord is chosen, along with corresponding airfoil width. One further aerodynamic design element that must be addressed is the number of airfoils per row.

$$\frac{\Psi_T}{p/_W} = 2\frac{\cos(\alpha_2)\cos(\alpha_1 + \alpha_2 - 90°)}{\cos(\alpha_1)} \quad \textbf{(5-10)}$$

Zweifel (1946) describes the relationship between the number of airfoils in a cascade and the performance losses. The resulting correlation is shown in Equation 5-10. The angles used in this equation can be absolute or relative depending on whether the stator or the rotor is being designed. According to Zweifel, the optimum value of 0.8 of the Zweifel parameter, Ψ_T,

minimizes losses. The pitch of each cascade is determined, and in some cases decreased in order to ensure the flow properly turned through the airfoil. The final number of airfoils in the stationary row is 30, and the number of rotating airfoils is 34. From this three-dimensional design a solid model is generated.

5.2 Aerodynamics Modeling with Computational Fluid Dynamics

The one-dimensional modeling method is now compared to a more complex SCO_2 fluid dynamics model. Modern computational software packages linearly solve Reynolds-averaging Navier-Stokes equations. The aerodynamics of the turbo-expander stage are solved by modeling the air solid in Solidworks and importing the solid for CFD into Star-CCM+.

5.2.1 Solid Modeling Technique and Meshing

The three-dimensional vane shape is modeled according to the one-dimensional design method. All of the airfoil profiles are sketched similarly to Figure 5-1 with the design parameters in Table 5-2. These profiles are stacked on each other according to the location of their centroid to minimize the centrifugal stress of rotating metal. A loft feature using these profiles in sequence creates the final airfoil three-dimensional shape. Figure 5-2 demonstrates a single vane and the entire assembly of vanes. The assembly of all the segments together creates a ring of 30 airfoils. The outer casing is varied according to the one-dimensional design and the change in density with the mean profile radius kept constant.

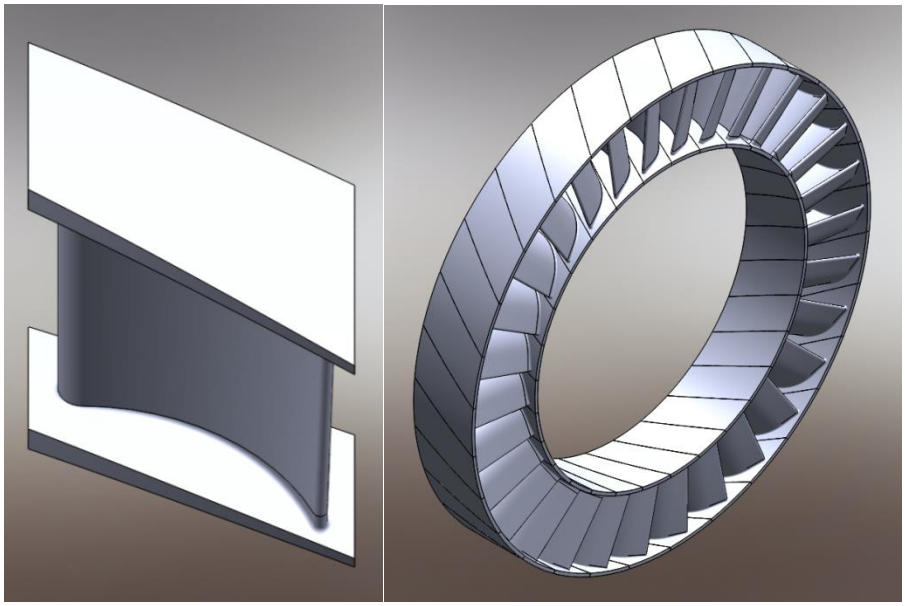

Figure 5-2: Turbo-expander stator individual segment and ring assembly

The rotor is also modeled in three-dimensional space. As seen in Figure 5-3, the blades as individual segments form a ring with 34 airfoils. This entire assembly will rotate at the prescribed speed and extract work from the flow.

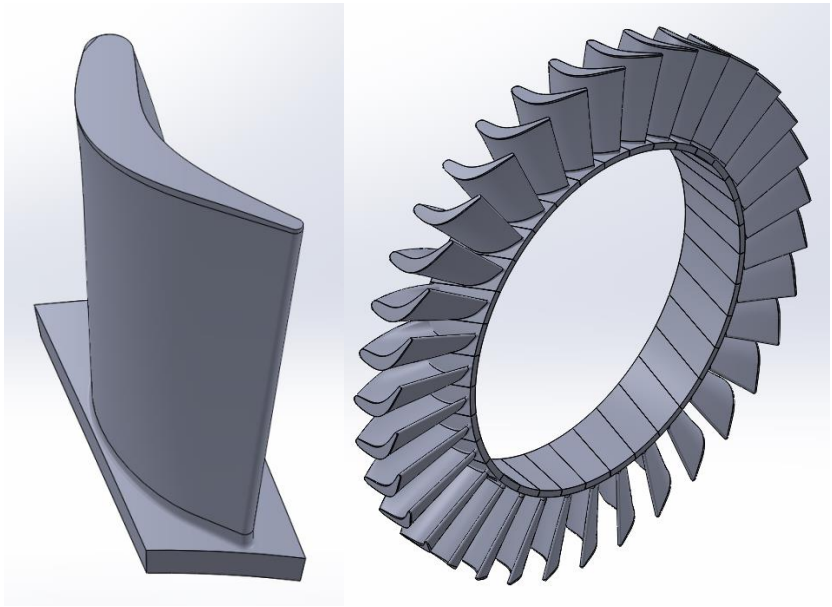

Figure 5-3: Turbo-expander rotor individual segment and rotating ring assembly

With the metal airfoils in a solid model, the flow surrounding them is formed into a solid body. A loft of the proper profile is made encompassing the airfoil, as displayed in Figure 5-4. Special care is made to give the airfoils enough space so that the periodic boundary cuts through flow in the center of the passage and does not affect the boundary of the airfoil. Also shown in the figure is the assembly of all the flow passages into a cohesive ring with no gaps at the edges. This indicates that the periodic boundary condition can successfully match the faces.

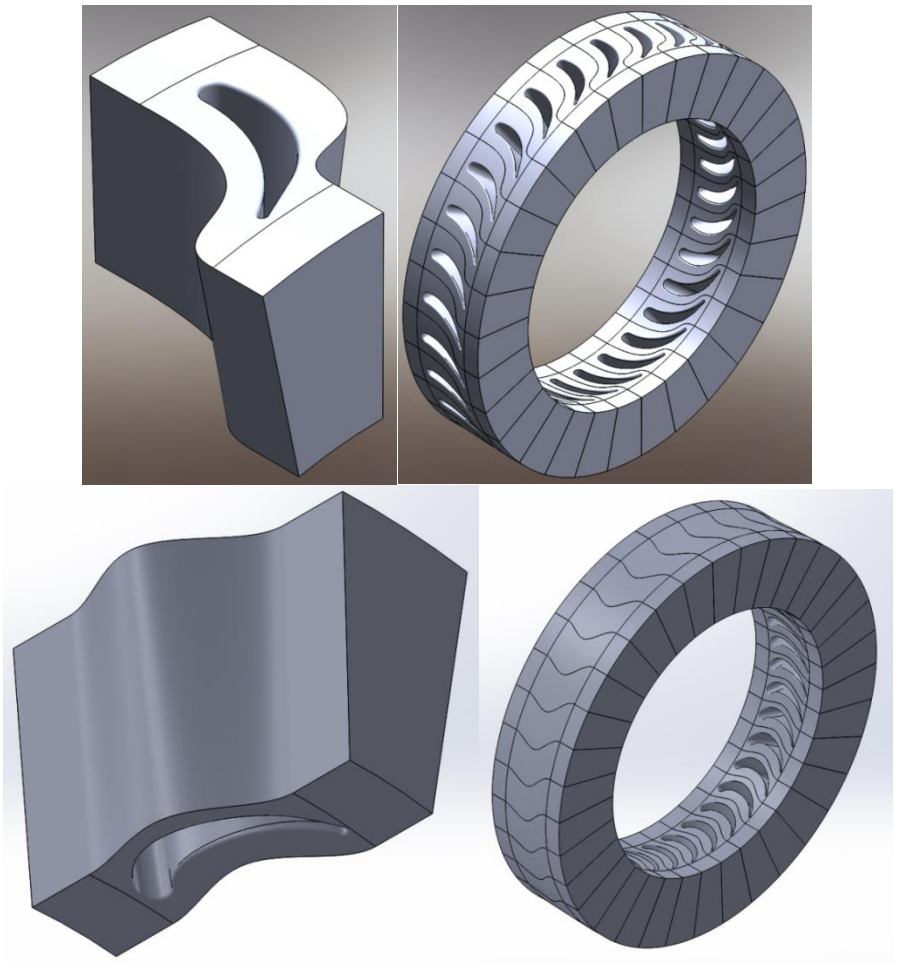

Figure 5-4: Flow model surrounding stator and rotor airfoils and periodic assembly

For the rotating airfoil, the tip is not shrouded so a gap of 1.52 mm of flow is included in the model. An additional 2 cm of flow model is extruded from the inlet and the outlet of each

airfoil. This is not necessarily indicative of actual spacing in the design engine, but it ensures that the CFD captures all relevant flow effects in that region.

Meshing is performed by the polyhedral and prism layer mesher built into Star-CCM+. The stator mesh, visualized in Figure 5-5, has approximately 2.66 million polyhedral cells. The prescribed base cell size is 0.6 mm. All faces are reported to be valid with no negative volume geometry. A target allowable cell quality of 0.8 is specified and the volume average quality of the final mesh is 0.73. For the volume change of cells, 99.6% experience a volume change of between 1.0 and 0.1, with no cells experiencing a volume change of 0.01. Eighteen prism layers surround the wall boundaries. The prism layer near the wall has a thickness of 10 nm and the remaining prism layers are scaled up in thickness until an overall thickness of 0.6 mm is achieved. The thickness near the wall brings the average wall y-plus to 0.11, with a maximum value of 0.56.

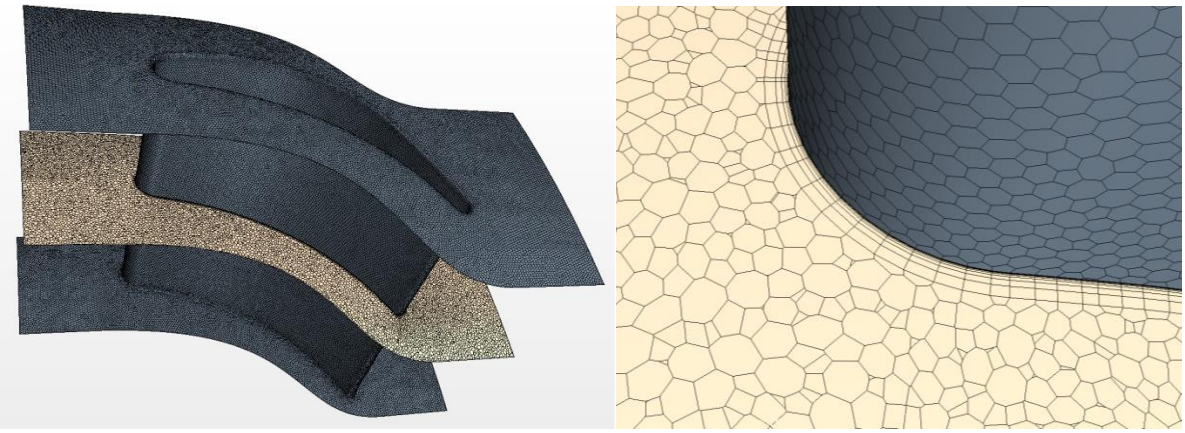

Figure 5-5: Stator mean-line slice of polyhedral mesh and prism layer mesh

For the rotating blade mesh, seen in Figure 5-6, the mesh contains approximately 2.46 million polyhedral cells. The target allowable quality during meshing is 0.8, with a volume average quality of 0.73 in the final mesh. All cells pass face validity tests. The volume change

falls on the order of 1.0 to 0.1 for 99.7% of cells with no cells having a volume change less than 0.01. A cell base size of 0.6 mm is specified. For the wall boundaries, 18 prism layers are used with an overall layer thickness of 0.5 mm. The layers are geometrically stretched with a first cell thickness of 5 nm. This small first cell thickness lowers the y-plus values on the walls. The average y-plus was 0.1 with a maximum value of 0.45.

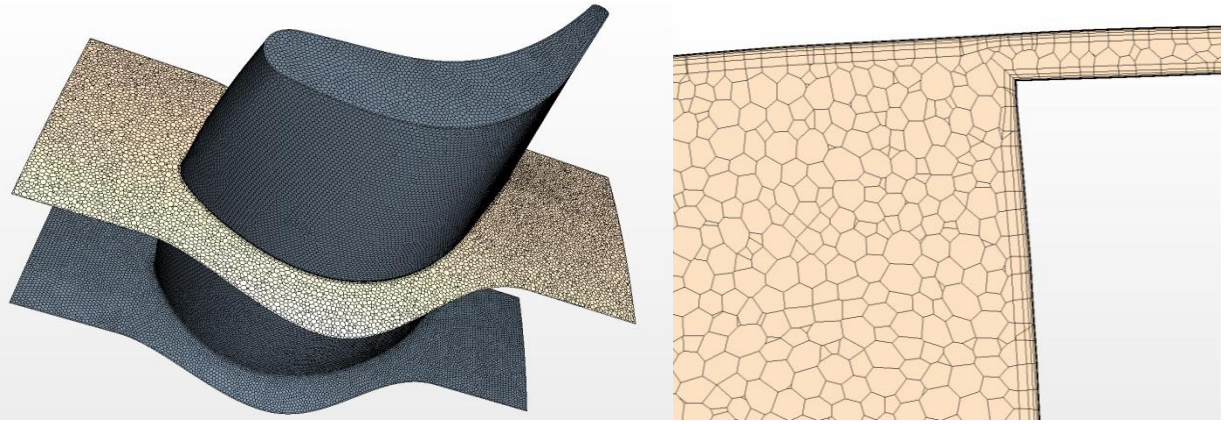

Figure 5-6: Rotor mean-line slice of polyhedral mesh and prism layer mesh

The boundary conditions are put in place to match the design specifications of the one-dimensional model. A mass flow inlet and a pressure outlet are used for both models. Once the stator converges, the variation from hub to casing of flow angle at the outlet is plotted. This variation is input as a field function onto inlet the boundary condition of the rotating airfoils. Only a single flow element is modeled and a periodic interface simulates the interaction from one airfoil to the next. The walls on the stator are stationary in the lab frame and adiabatic. The walls on the rotor airfoil and hub experience an imposed rotating condition of 8700 RPM. The casing surface is set to be stationary in the lab reference frame. All walls in the rotor have an adiabatic boundary condition.

The physics continuum is the key aspect of modeling SCO_2 in CFD through these airfoils. The fluid is modeled as a real gas with coupled energy and flow. It is assumed to be at a steady state with the SST model governing turbulence. Because the thermodynamic property variation in the turbo-expander does not depend on pressure, tables dependent on temperature only are generated for specific heat, thermal conductivity, and viscosity. The Peng-Robinson modification of the real fluid model is used as an equation of state for the physics continuum.

5.2.2 Turbo-Expander Stator CFD Results

The simulation is run in Star-CCM+ and convergence is considered achieved after the values of calculation residuals fall beneath 0.001. For the stator model, this occurred after approximately 1800 iterations. The mass flow at the outlet deviates by less than 0.01%.

Table 5-3: Averaged results at the inlet and outlet of the stator CFD

	Inlet	Outlet
Total Pressure (MPa)	24.12	23.97
Static Pressure (MPa)	23.71	21.11
Total Temperature (K)	1353.6	1353.6
Static Temperature (K)	1350.4	1329.4
Velocity Magnitude (m/s)	95.58	259.0
Flow Angle (º)	0.00	67.67

Table 5-3 shows the average results of the stator CFD simulation at the inlet and the outlet. A mass flow averaged method is used to extract the averages from the CFD model. The averaging is done across the inlet and the outlet plane, which are parallel to the r-θ plane. This approach of mass flow averaging is used for all other CFD fluid property averages in this study.

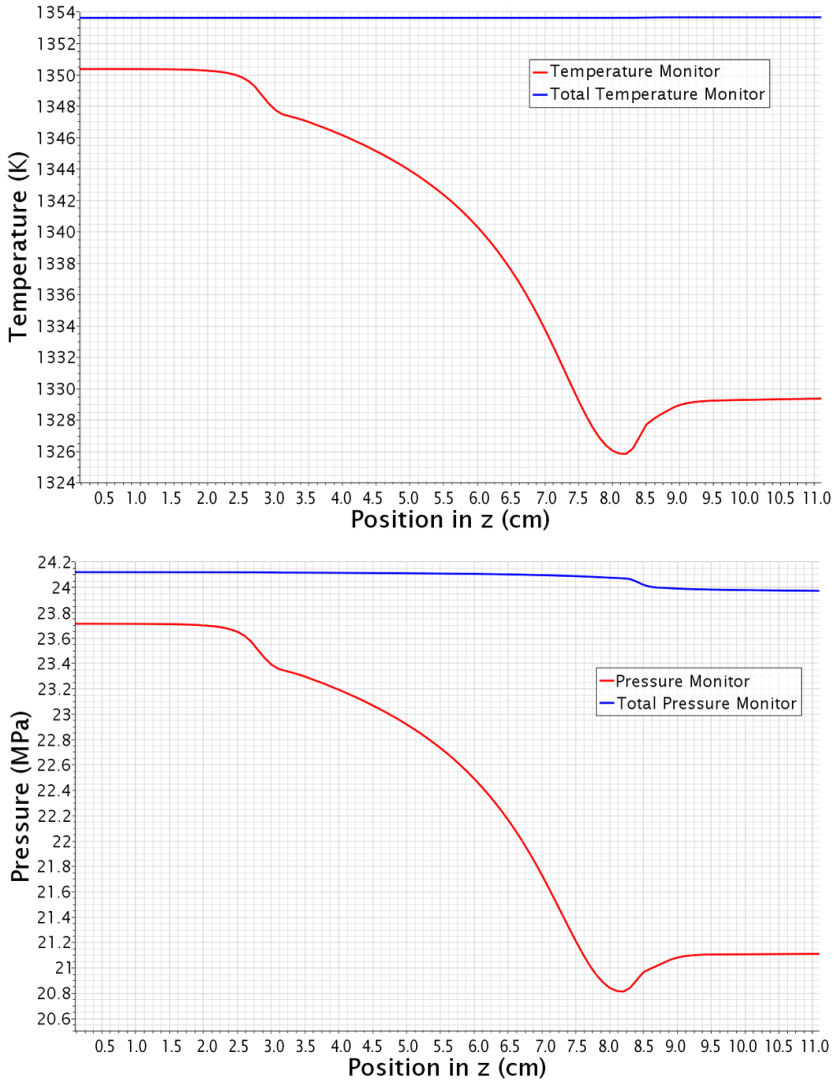

Figure 5-7: Stator average temperature and pressure

Figure 5-7 shows the average temperature and pressure in the r-θ plane as a function of the position of that plane in the z direction. The first and last 2.0 cm of the model show no major changes in properties because that region is the constant area inlet and outlet portion. The total temperature is constant, which is expected for an adiabatic airfoil. Sudden dips in the average temperature and pressure are observed at the leading and trailing edge of the airfoil. The total pressure experiences a noticeable drop across the airfoil due to losses. The total and static

enthalpies are also monitored, but the trend is nearly identical to the temperature graph, so it is not shown here.

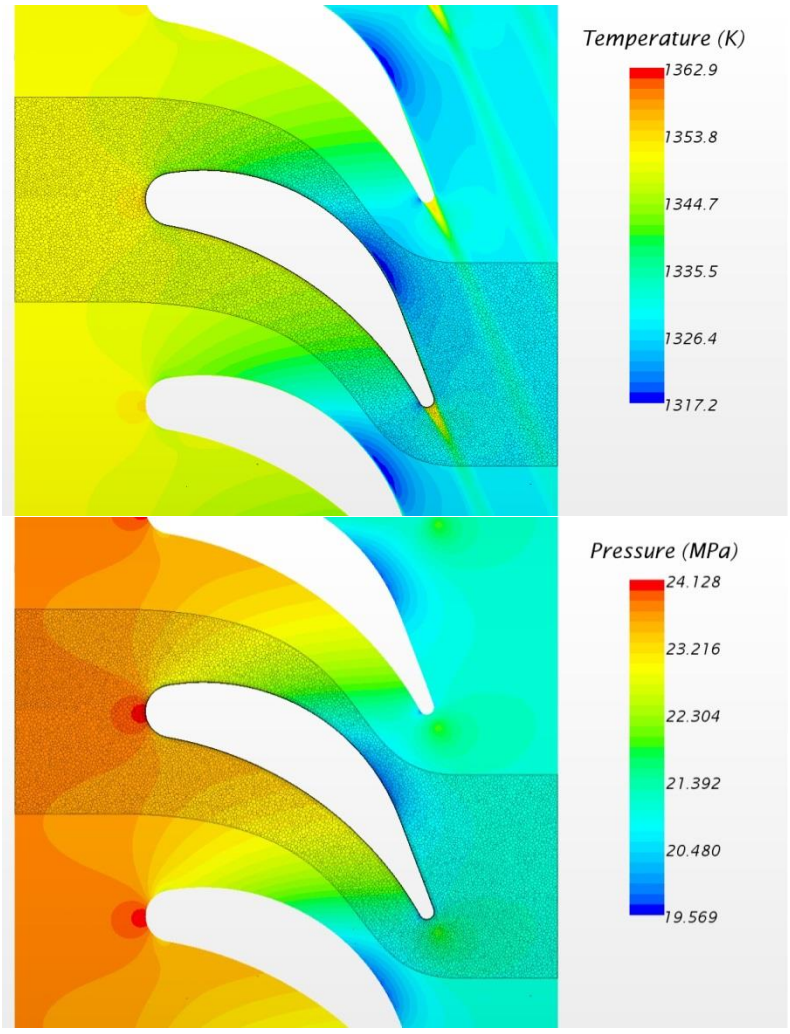

Figure 5-8: Stator temperature and pressure at the mean-line

The temperature and pressure variation at the mean-line through the stationary airfoil cascade is shown in Figure 5-8. This chart is also a good indicator of trends in velocity. Where the pressure builds up at the leading edge, the flow is stagnating. At the most constrictive point in the airfoil cascade, the flow velocity is highest and the pressure is lowest. The mesh of a single fluid slice is overlaid so that the boundaries of the domain are known. There do not appear to be

any effects following the edge of the fluid boundary, and so the periodic condition is not creating any noticeable artificial effects that can skew results.

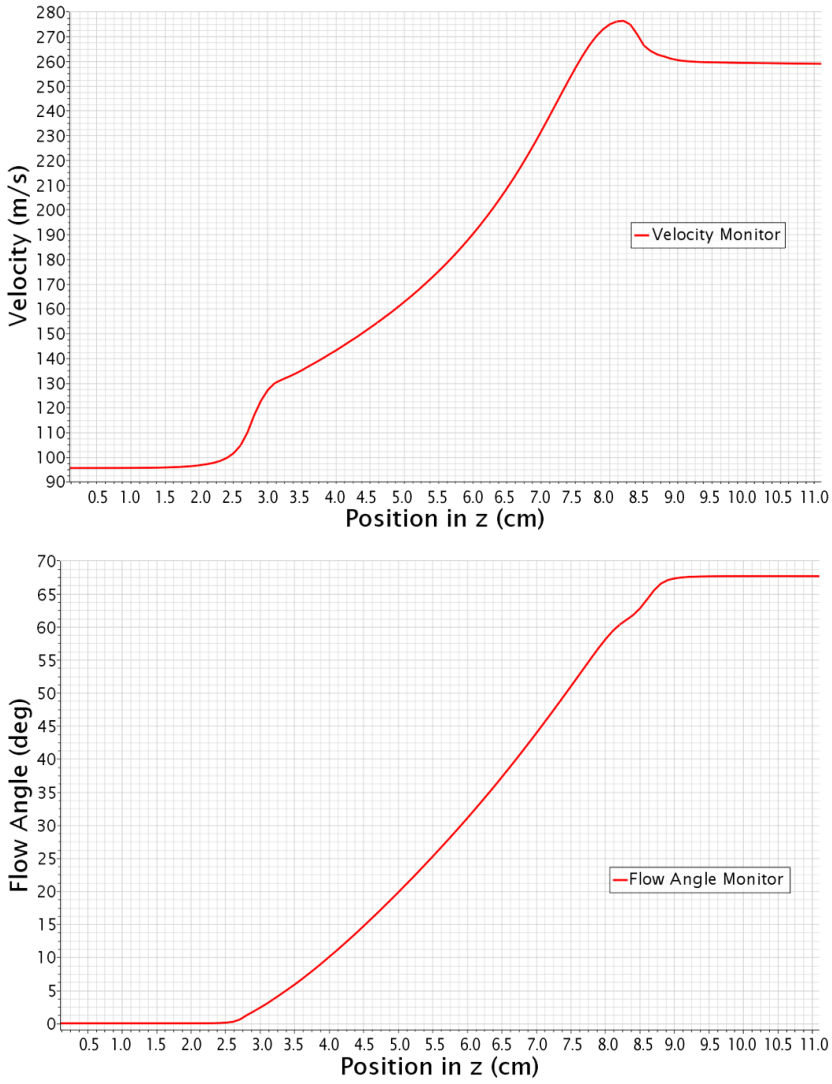

Figure 5-9: Stator average flow velocity and angle

The trends in velocity magnitude and angle, seen in Figure 5-9, follow expected trends. The angle roughly linearly reaches its final value, but the flow velocity builds in an almost exponential way once it is in the airfoil passage. This trend is due to the cross sectional passage between airfoils changing with the thickness of each airfoil. The trend in this cascade is

acceptable, but if a different change in average velocity is desired, this method can be used to inform the shape of the airfoil passage.

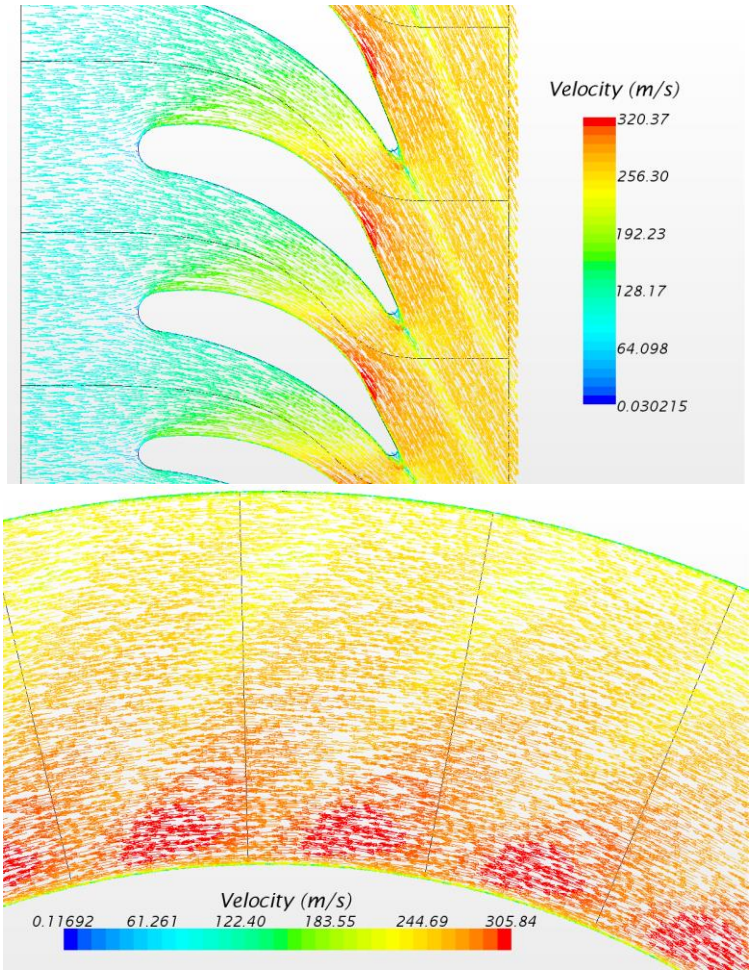

Figure 5-10: Stator velocity at the mean-line and exiting the cascade

The behavior of the flow's velocity is displayed in Figure 5-10. In the mean-line view, the flow stagnates at the leading edge. The flow then splits and gradually increases through the constriction of the passage. The trailing edge creates a zone of low velocity. The low pressure caused by this zone may help bias the flow to have a shallower angle than the design case. This loss can be mitigated by increasing the design angle or reducing the radius at the trailing edge. The flow exiting the stationary row goes from faster to slower from the hub to the casing. The

zones of low velocity due to the trailing edge can also be seen. The velocity swirls in a counterclockwise direction according to this view. Thus, the qualitative shape of the flow meets the requirements of the one-dimensional design, including the radial equilibrium specification with free vortex flow.

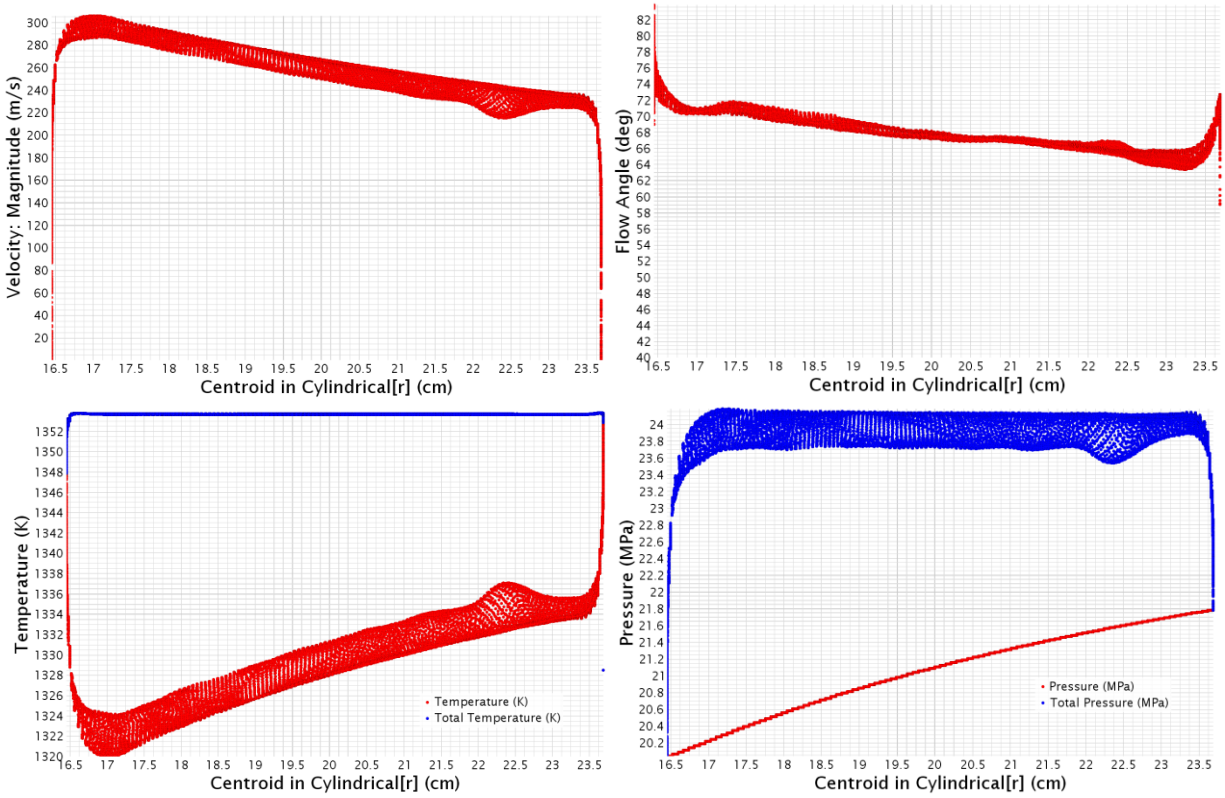

Figure 5-11: Stator outlet velocity, flow angle, temperature, and pressure

Figure 5-11 shows the general trends of the flow at the outlet of the stator as measured from hub to casing. The velocity decreases, as expected. The angle in velocity is also decreasing, following the expected trends. The total temperature remains constant due to the adiabatic boundary condition. The total pressure trends downward from hub to casing. This could be caused by greater losses near the casing surface.

5.2.3 Turbo-Expander Rotor CFD Results

Using the trends from Figure 5-11, the variation in flow angle and temperature with radius is applied to the inlet boundary condition through a field function. The mass flow through the turbo-expander is divided by the number of rotors, 34. The rotating airfoil is considered converged when all the residual elements fell beneath 0.001. For the rotor, this criterion is met within approximately 1600 iterations.

Table 5-4: Averaged results at the inlet and outlet of the rotor CFD

	Inlet	Outlet
Total Pressure (MPa)	23.84	20.26
Relative Total Pressure (MPa)	21.67	21.48
Static Pressure (MPa)	21.11	19.81
Total Temperature (K)	1352.3	1323.1
Relative Total Temperature (K)	1334.1	1334.1
Static Temperature (K)	1329.1	1318.8
Relative Velocity (m/s)	115.6	204.1
Velocity Magnitude (m/s)	253.3	107.3
Relative Flow Angle (º)	23.21	59.34
Flow Angle (º)	67.02	4.21

Again, the CFD model is used to average the fluid conditions at the inlet and outlet of the domain and displayed in Table 5-4. Because the airfoils are rotating, the relative values of velocity, flow angle, total temperature, total pressure, and total temperature are also averaged and tabulated. The method for averaging each attribute follows the same conventions outlined for the stationary airfoils.

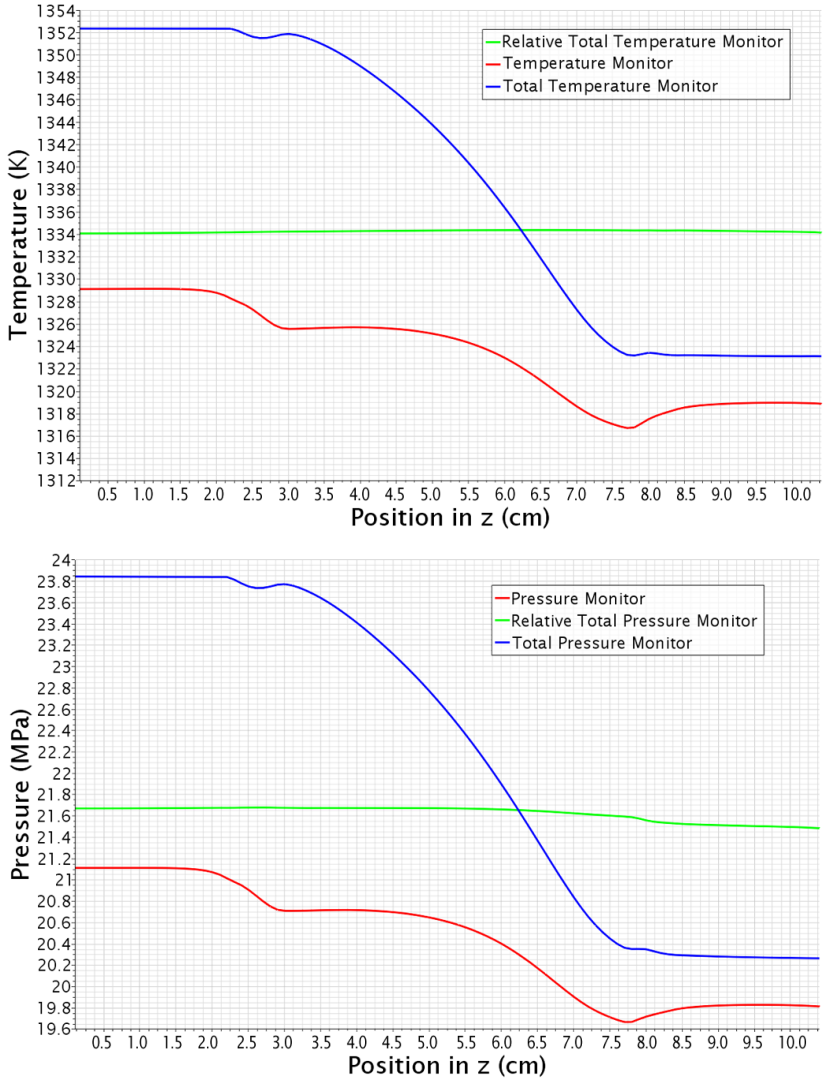

Figure 5-12: Rotor average temperature and pressure

Figure 5-12 shows the change in temperature and pressure across the rotor in the axial direction. Because the airfoil is considered adiabatic, total temperature remains constant, but this time in the relative reference frame. The trend in relative total pressure has a slight increase, similar to the behavior to the total pressure in the stator, seen in Figure 5-7. Overall, the trend in the rotor is similar to the stator where the static temperature and static pressure drop across the cascade.

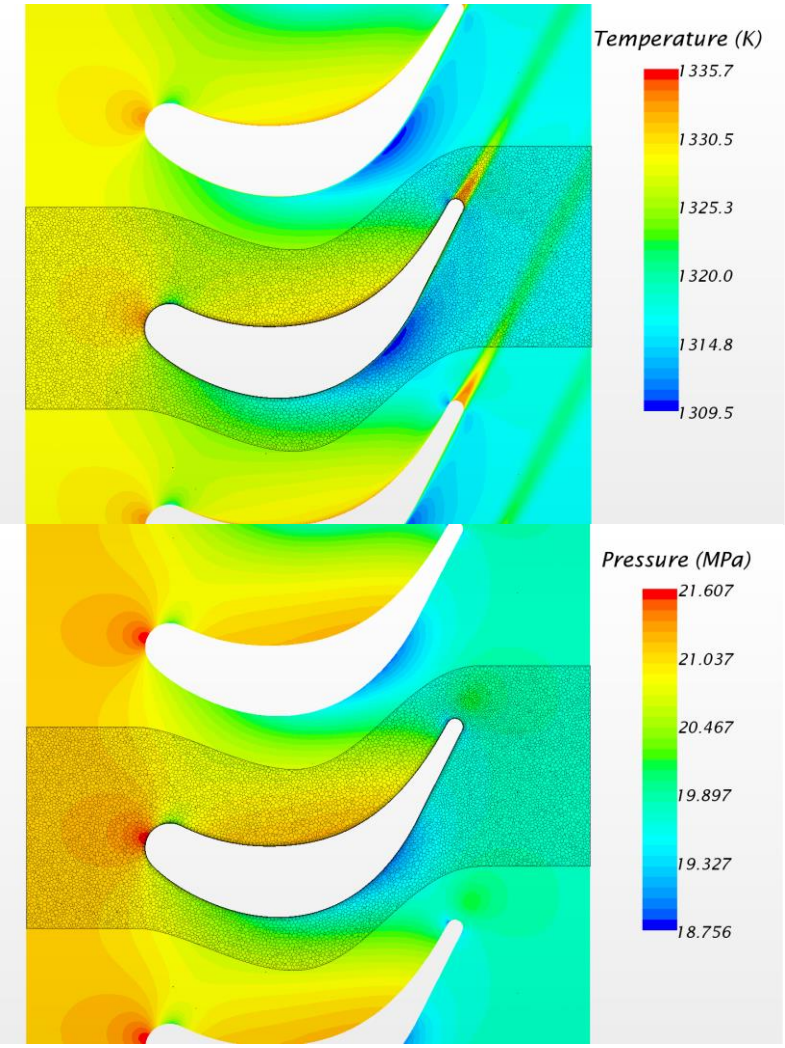

Figure 5-13: Rotor temperature and pressure at the mean-line

The variation of pressure through the passage, demonstrated in Figure 5-13, follows expected trends. The side receiving the flow experiences the highest pressure, known as the pressure side. The opposite side has the lowest pressure gradients; it is called the suction side. There is a small region of low pressure near the leading edge of the rotor. This is due to the angle of incidence not properly matching the intended design angle of the airfoil. When the rotor simulation's boundary conditions are set, the inlet flow angle is matched to the outlet flow angle from the stator. Thus, the stator is not producing a large enough turn in the flow to successfully

reduce the angle of incidence, creating further loss in the rotor. The angle of incidence is, on average, 13.33°, the final analysis will show if this additional loss will significantly impact performance

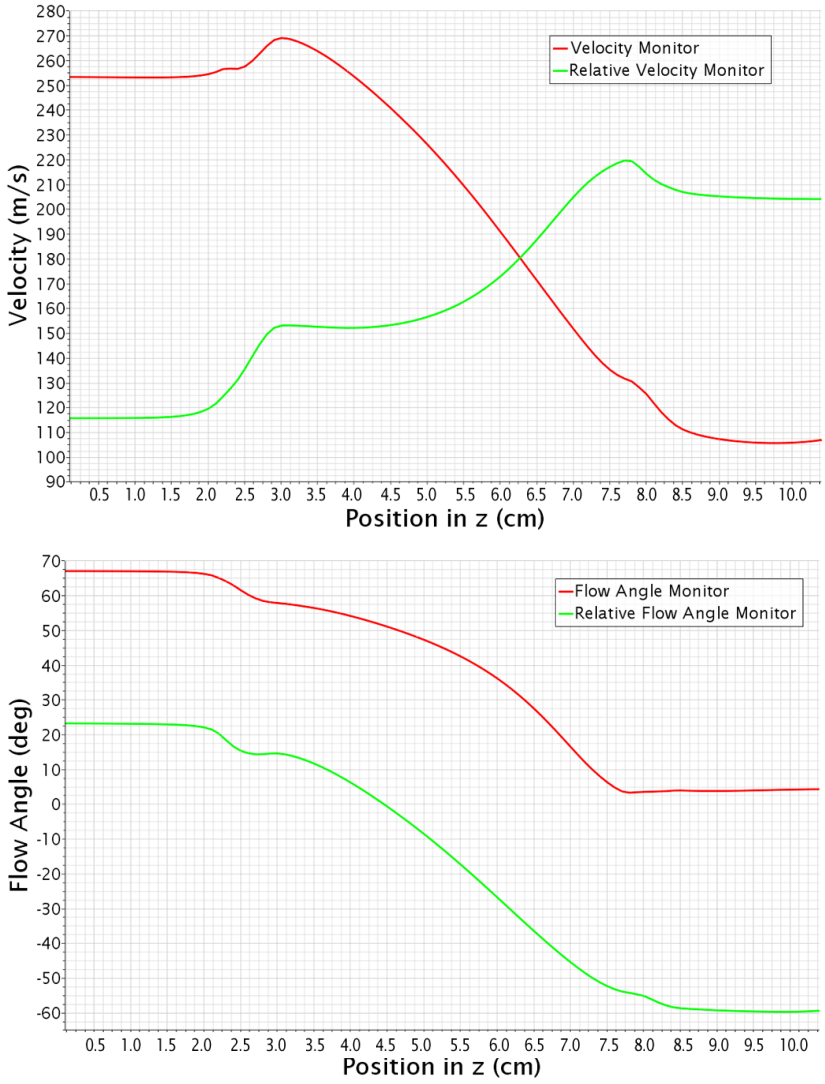

Figure 5-14: Rotor average flow velocity and angle

The average variation of velocity characteristics in the axial direction are charted in Figure 5-14. As the flow increases in magnitude in the relative frame, so the angle begins turning in the opposite direction. Because the axial flow component of velocity is constant, the relative

flow direction changes from a downward to an upward direction when the flow angle is reported as negative. The turning of the relative flow at the mean-line can be seen the top-right diagram in Figure 5-15. However, when the relative flow is brought into the stationary reference frame, it has significantly slowed down and has a small, positive angle. This behavior is charted in Figure 5-14, and visualized in the top-left diagram of Figure 5-15

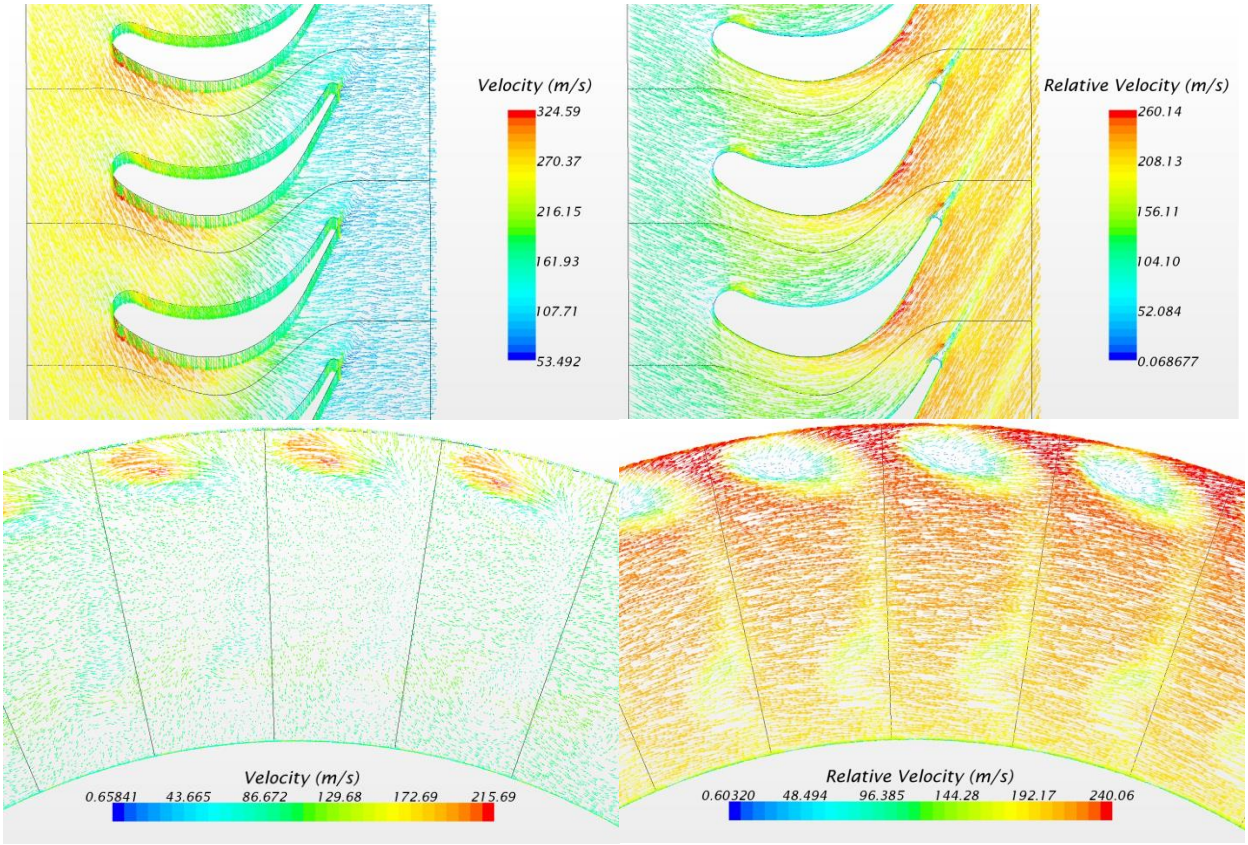

Figure 5-15: Rotor velocity and relative velocity at the mean-line and exiting

The behavior of the flow in Figure 5-15 confirms that Star-CCM+ is correctly applying the rotating boundary condition to all rotating surfaces. The stationary and relative frame velocities at the exit of the rotating airfoil show a potential source of loss at the airfoil tip. The small tip gap at the top of the airfoil created an area of trapped, stagnated flow. This flow did not

get properly turned by the airfoil into point in correct direction. As a result, when the flow slips over the end of the trailing edge it will not be properly conditioned and create a loss.

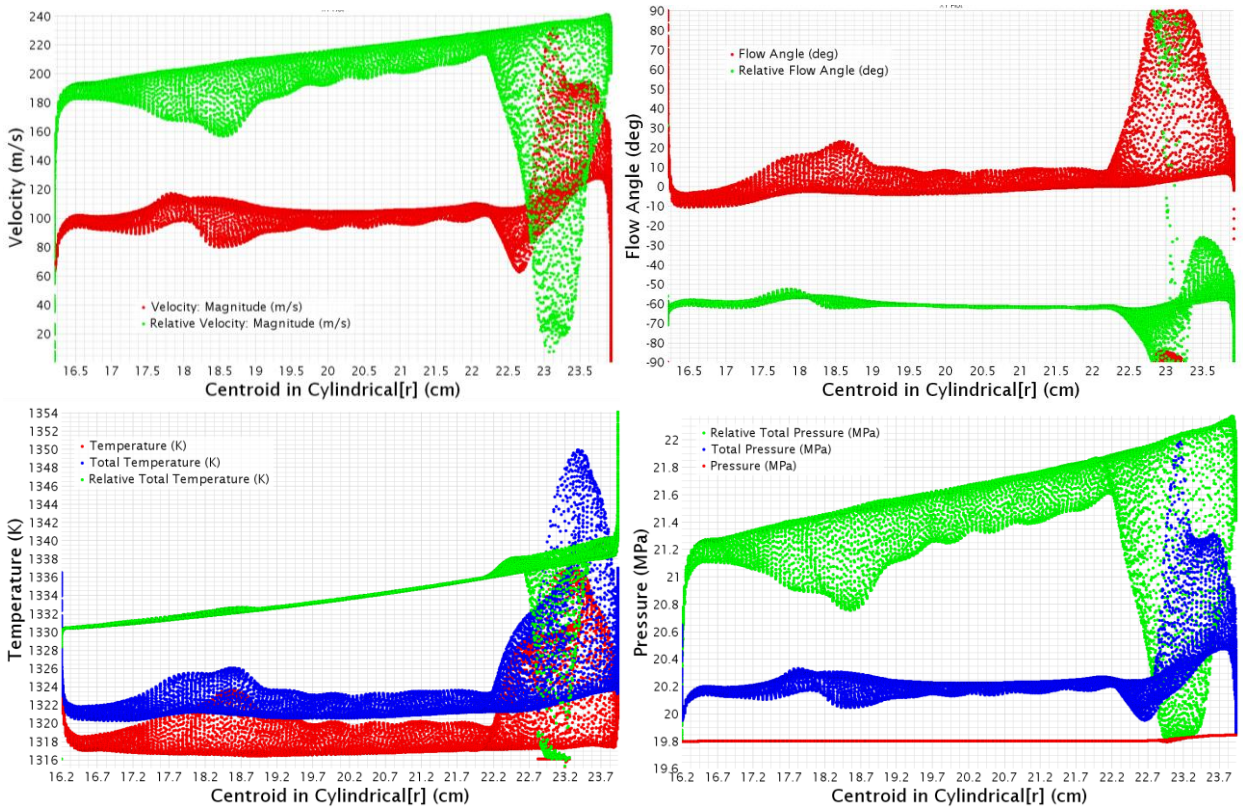

Figure 5-16: Rotor outlet velocity, flow angle, temperature, and pressure

Figure 5-16 demonstrates the trend in velocity, temperature and pressure at the exit plane of the rotating airfoil. The wild variation in flow properties near the casing represents the tip gap effects. The temperature and pressure both appear to have an even trend without much variation in annular radius. This is an indicator that the trend in the model matches the design trend. In the one-dimensional design, the exit flow angles do not vary from hub to casing by a significant amount. Thus the intent of the one-dimensional design was achieved.

6 HEAT TRANSFER: MODELING A RECUPERATIVE HEAT EXCHANGER

The RRC gains significant efficiency through the transfer of heat from the low pressure carbon dioxide to the high pressure fluid. Often, due to the low pressure ratios, the heat load required to be recuperated back into the cycle is much greater than the heat being added or rejected from the cycle. Therefore, the recuperator performance is more crucial than that of the heater or the cooler. The recuperator must also be robust enough to withstand high pressure fluids, and its material must perform within a wide range of temperatures. The modeling of heat transfer in a heat exchanger with SCO_2 can be difficult because the properties can vary widely and gain pressure dependence as the fluid approaches the critical point

6.1 Modeling Through Discretization into Control Volumes

The analytical modeling approach in the heat exchanger requires an initial exchanger concept. SCO_2 requires large pressures to operate an efficient power cycle. In the design of a heat exchanger, the channels must withstand the stress placed on them by the pressure differential from the hot to the cold fluid. A classic shell-and-tube heat exchanger suspends pipes in a pressure vessel. The wall thickness of the suspended pipes would need to increase to withstand the pressure difference between the two vessels. This is bad for heat transfer. Heat exchangers with millimeter scale or smaller channels are now being produced (Carman, 2002), and they provide an attractive solution for a SCO_2 power cycle. The small channels distribute the

force so that the walls do not need to be as thick, allowing for better, more compact heat exchangers.

A heat exchanger channel configuration is conceived that has alternating, square channels in counter-flow. The fluid enters through a manifold that distributes the flow between many rows of these channels and through the shape transitions the fluid into the alternating square pattern. The HTR and the LTR are the heat exchangers targeted in this modeling study. These components have the highest heat load requirement, and so their performance significantly affects the overall efficiency of the cycle. Millions of these channels will be required to provide enough heat transfer between fluids. In this heat exchanger design, Inconel 625 is selected as the wall metal because of its ability to withstand hot temperatures.

6.1.1 Heat Exchanger Analytical Modeling Method

Because the properties of SCO_2 are changing across the length of these heat exchangers, a discretization method is adopted for the one-dimensional heat transfer model. Figure 6-1 provides a visual example of how the one-dimensional model operates. The heat exchanger cross section contains small square channels that are split lengthwise into distinct control volumes. Each control volume feeds into the next control volume through an iterative method until the entire heat exchanger is solved. This method for solving small channeled heat exchangers is derived from a similar approach by Carman (2002).

Heat transfer from one channel to the next is modeled through a resistive thermal circuit. In the recuperators the hot fluid, which is at a lower pressure, supplies the heat energy to the cold fluid, which is at a high pressure. Because the properties rapidly change as the temperature gets

cooler in these exchangers, the control volumes must be small enough to capture this change. The one-dimensional model assumes that the change in temperature and properties is approximately linear in each control volume. With this assumption the average value of each fluid property can be read from the REFPROP database at the average temperature and pressure. The lateral heat conduction through the metal is also accounted for, and this represents a loss of heat from the hot fluid that could have been supplied to the cold fluid.

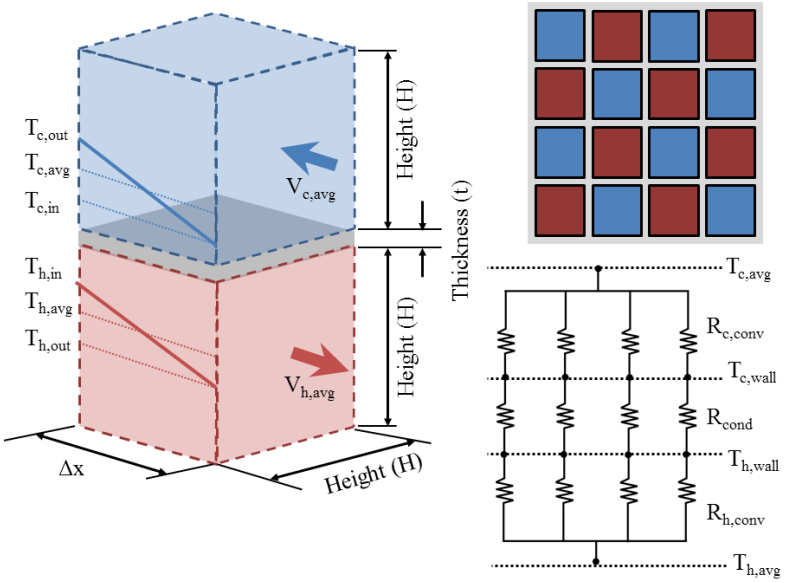

Figure 6-1: Heat exchanger channels and control volume modeling method

Equation 6-1 and Equation 6-2 explain the update method in the code for the temperature and pressure of the fluid. First, a delta temperature and pressure across the control volume is assumed. This is used to update all property values and calculate the heat transfer. The heat transfer from the hot fluid to the cold fluid updates the actual average temperature of the fluids, walls and pressures leaving the control volume. These values are usually different from the initial temperature and pressure change assumption. The equations are updated with more

accurate guesses of the fluid change across a control volume. This must be repeated several times until the guessed fluid state change agrees with the calculated change by less than the thousandth decimal place. When this criterion is met the solution is considered converged.

$$T_{n,avg} = T_{n,in} - \frac{\Delta T_n}{2} \quad \textbf{(6-1)}$$

$$P_{n,avg} = P_{n,in} \pm \frac{\Delta P_n}{2} \quad \textbf{(6-2)}$$

The Reynolds number, defined in Equation 6-3, of each channel is dependent on the number of channels chosen for design. The mass flow is split equally among all the channels. The length scale of the Reynolds number is the hydraulic diameter of the square channel. Viscosity, as with all fluid property values, is updated on a per-control-volume basis using the average temperature and pressure.

$$Re_{avg} = \frac{\dot{m}_{\ channel} D_{hyd}}{s^2 \mu} \quad \textbf{(6-3)}$$

The average channel Nusselt number is found with the Dittus-Boelter correlation, Equation 6-4, for turbulent flow convective heat transfer. In this relationship, the Prandtl number is raised to the power 0.3 for the hot fluid and raised to the power 0.4 for the cold fluid. After the Nusselt number of each control volume is modeled, the average heat transfer coefficient is determined using Equation 6-5. This value is later used in the heat transfer circuit to update the temperatures of the fluids and the metals.

$$Nu_{avg,n} = 0.023\ {Re_{avg}}^{0.8} Pr^a \quad \textbf{(6-4)}$$

$$h_{o,avg,n} = \frac{k_f Nu_{avg}}{D_{hyd}} \quad \textbf{(6-5)}$$

Each individual control volume can be treated as a heat exchanger with constantly changing properties. The logarithmic mean temperature difference (LMTD) approach is used to find the heat transfer within a control volume. Equation 6-6 lays out the calculation required to find the LMTD in each control volume.

$$LMTD_n = \frac{(T_{h.n} - T_{c,n}) - (T_{h.n} - \Delta T_{h,n}) + (T_{c.n} - \Delta T_{c,n})}{\ln((T_{h.n} - T_{c,n})/((T_{h.n} - \Delta T_{h,n}) - (T_{c.n} - \Delta T_{c,n}))} \quad \textbf{(6-6)}$$

Next, Equation 6-7 is implemented, and the LMTD is used to evaluate the heat transfer from the hot fluid, through the metal, and into the cold fluid. The control volume approach allows the heat transfer through one wall of the heat exchanger to be found and then scaled up by multiplying by the total number of walls of heat transfer within the heat exchanger. Thus, the heat transfer in the entire heat exchanger for one control volume length, Δx, is modeled.

$$\dot{Q}_{f,n} = \frac{N_w \times LMTD_n \times \Delta x \times s}{\left({}^{1}/_{h_{h,n}} + {}^{t}/_{k_{mat}} + {}^{1}/_{h_{c,n}}\right)} \quad \textbf{(6-7)}$$

$$\dot{Q}_{lat,n} = N_w \times t \times s \times k_{mat} \frac{T_{wall,n} - T_{wall,n+1}}{\Delta x} \quad \textbf{(6-8)}$$

$$\dot{Q}_{total,n} = \dot{Q}_{f,h,n} + \dot{Q}_{lat,n-1} - \dot{Q}_{lat,n} \quad \textbf{(6-9)}$$

Because the entire heat exchanger has millions of channels, lateral conduction of heat through the metal has a small, but noticeable effect. The lateral conduction will travel from the hot end to the cold end. The exchanger is considered to be well insulated on the outside walls, so the conduction from the center channels to the outside channels is assumed to be negligible. Fourier's Law is modified for this application in Equation 6-8. It predicts the lateral conduction across a single wall of heat exchange and multiplies it by the total number of walls. Once the lateral heat loss is known, the Equation 6-9 gives total heat balance in the control volume. The

approach to the total heat transfer uses the metal wall as a control volume, solving for the total energy added to the cold fluid.

$$T_{wall,n} = \frac{\dot{Q}_{total,n}}{N_w} \times \frac{1}{h_{o,avg,n}\, s\, \Delta x} \tag{6-10}$$

$$T_{f,n+1} = T_{f,n} - \frac{\dot{Q}_{total,n}}{\dot{m}_{total}\, c_p} \tag{6-11}$$

The driving temperature in lateral heat conduction is the average wall temperature from one end of the control volume to the other. The method by which the wall temperature is calculated is described by Equation 6-10. Once a control volume section is solved for, the temperature of the fluid entering the next control volume must be updated so that the code can be iterated to convergence. The method for updating fluid temperature is in Equation 6-11. Treating the fluid channels as a control volume, the change in temperature across the control volume is dictated by the net heat and the average fluid specific heat capacity.

$$\frac{1}{\sqrt{f_n}} = -2\log_{10}\left(\frac{\varepsilon_o}{3.7 D_h} + \frac{2.51}{Re_n\sqrt{f_n}}\right) \tag{6-12}$$

$$P_{n+1} = P_n \pm f_n \frac{\Delta x}{D_{hyd}} \frac{(\dot{m}_{channel})^2}{2\, s^4\, \rho} \tag{6-13}$$

The Darcy-Weisbach equation, Equation 6-13, describes the pressure drop in a channel across a control volume. The Darcy friction factor, required to understand the pressure drop, is solved for through the Colebrook relation, shown in Equation 6-12. Through these two methods, the pressure drop across a control volume is iteratively solved. The roughness of the heat exchanger walls depends on the material and manufacturing method used. In this case, Inconel 625 is the selected heat exchanger metal.

$$\sigma_{b,max,n} = \frac{\left(P_{c,avg,n} - P_{h,avg,n}\right) s^2}{2\, t^2} \times 10^{-6} \quad \textbf{(6-14)}$$

$$\sigma_{b,thermal,n} = \frac{E \alpha_t \left(T_{h,mat,n} - T_{c,mat,n}\right)}{2} \times 10^{-6} \quad \textbf{(6-15)}$$

As stated before, the stress on the metal between the high pressure fluid and the low pressure fluid is a critical design limitation. The stress on a wall in the control volume is modeled as a simple beam, clamped on both ends. The difference in pressure, according to the Zhuravskii formula in Equation 6-14, contributes to bending stress, along with the thickness of the wall and the surface area of pressure. There is also a temperature difference between the wall on the cold side and the wall on the hot side. This causes beam bending following the relationship in Equation 6-15. The material properties in these equations vary with temperature. To capture this effect, the average wall temperature across a control volume is used in these equations. The beam expands the most on the hot side, which is also the low pressure side. Because of this, the pressure induced bending and the thermal bending stress are additive. A minimum factor of safety of 2 is chosen as the design limit for the entire heat exchanger.

The selection of an optimum design depends on the balance of design factors. Making the channels smaller allows the walls to be thinner by the material stress limit. But the tiny channels increase the Reynolds number to the point where the pressure losses become too large. Thicker walls between channels force the heat exchanger to lengthen in order to meet the required heat load. This also dramatically increases the volume of metal needed to construct the heat exchanger, driving up the cost. All of these factors are balanced, changed, and iterated until the heat exchanger performs to the standards required by the original cycle design while achieving the lowest volume of material possible.

6.1.2 Optimized Heat Exchanger Design

The physical specifications of the HTR and the LTR one-dimensional design model are reported in Table 6-1. Each channel is approximately 1.4 mm wide and the walls between channels are about 0.3 mm thick. The HTR requires 2.8 million channels, whereas the LTR specifies 1.4 million channels. The HTR is a 3 meter by 3 meter by 4 meter rectangular solid, and the LTR is approximately a 2 meter cube. The material volume requirement is lower in the LTR, however its heat load is also much lower. Control volumes of a length of about 6.6 mm are sufficient to model the heat exchanger.

Table 6-1: Optimized recuperator physical design parameters

	HTR	LTR
Number of channels	2,755,600	1,440,000
Channel side, s (mm)	1.48	1.44
Wall thickness, t (mm)	0.350	0.335
Number of control volumes	600	300
Control volume length, Δx (mm)	6.589	6.676
Square exchanger side (m)	3.037	2.112
Channel overall length (m)	3.953	2.003
Metal material volume (m^3)	12.71	3.19

For this sizing of the HTR and the LTR, the modeled performance is listed in Table 6-2. The maximum stresses are well within the safety factor of the material. The wall between the channels does experience some deflection, but only by 0.016% of the channel side. Thus, the flow is not constricted in a significant way. The pressure drop is approximately is specified in the cycle design. The heat transfer goals are met according to the optimized cycle.

Table 6-2: Optimized recuperator performance parameters

	HTR	LTR
Maximum bending stress (MPa)	129.7	132.8
Maximum beam deflection (μm)	0.231	0.249
Hot Side Pressure drop, $\Delta P/P_{in}$	0.505%	0.494%
Cold Side Pressure drop, $\Delta P/P_{in}$	0.083%	0.036%
Total heat exchange (kW)	618,850	92,151
Lateral heat transfer (kW)	1.759	0.584
Overall heat transfer coefficient, Uo	850.4	1097
Effectiveness	0.986	0.912

The effectiveness of the HTR and LTR are also close to the cycle optimization prediction. A pinch point of 10 K is reached in both heat exchangers. The lateral heat conduction is reported for both exchangers, but it is not significant compared to the overall heat load.

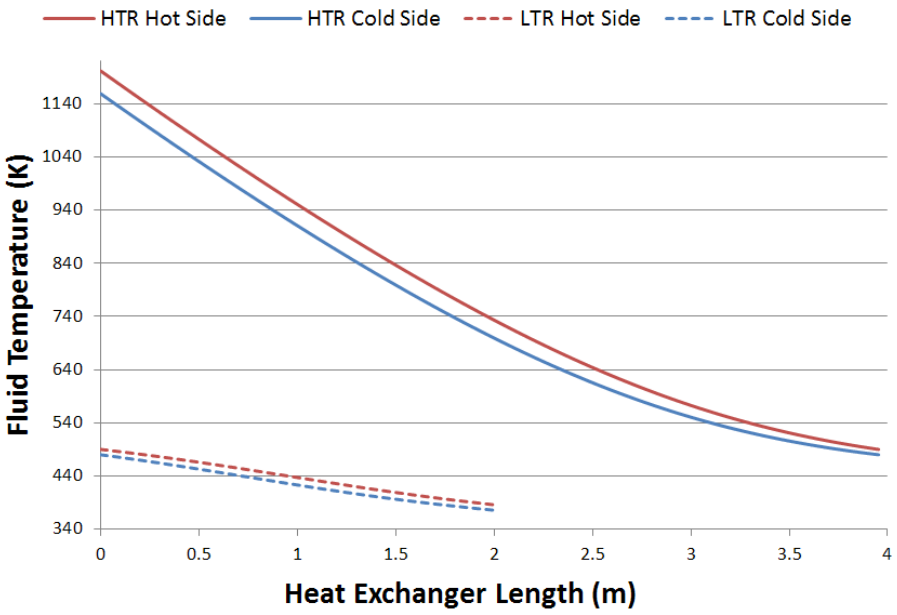

Figure 6-2: Fluid temperature vs length of the recuperator

Figure 6-2 charts the temperature change in the fluid for the counter-flow recuperators. As expected for the HTR, the pinch point occurs at the coldest end. The furthest separation in fluid temperatures happens at the hot end, with a split of 42.86 K. The LTR, however, is essentially pinched at both ends, although the hot end has the temperature difference of 10.0 K, whereas the cold end has a temperature difference of 10.2 K. The highest temperature differential, 14.1 K, occurs near the middle of the LTR at a length of 0.96 m.

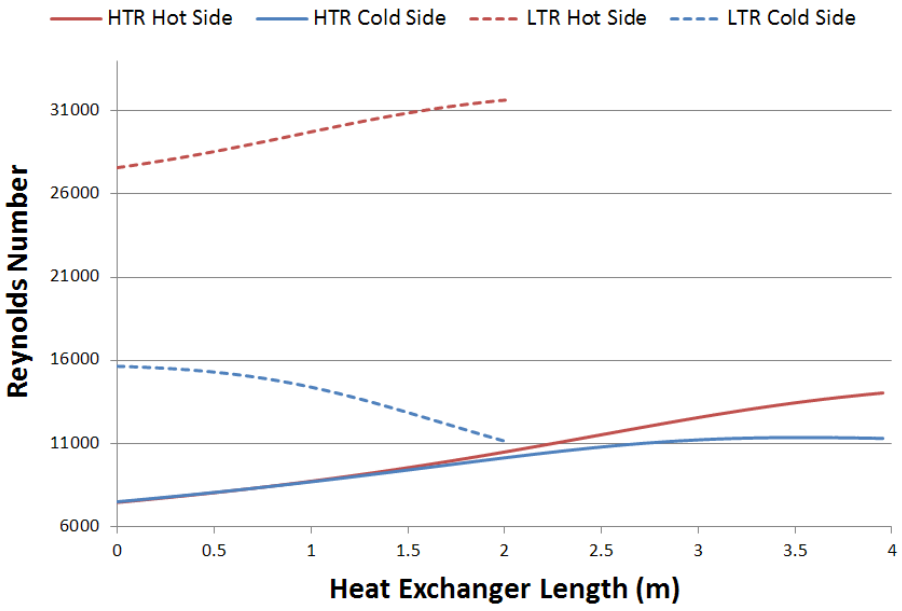

Figure 6-3: Fluid Reynolds number vs length of the recuperator

The behaviors of Reynolds number for the LTR and HTR are graphed in Figure 6-3. The behavior of viscosity near the critical point contributes to the shift in curvature in the Reynolds number. Also, the cold side of the LTR accepts flow directly from the main compressor with a mass flow rate of 504.7 kg/s. The difference in mass flow rates forces the heat exchanger channels wider than they would need to be if the mass flow rates are equal. The pressure drop must be balanced with the Reynolds number difference.

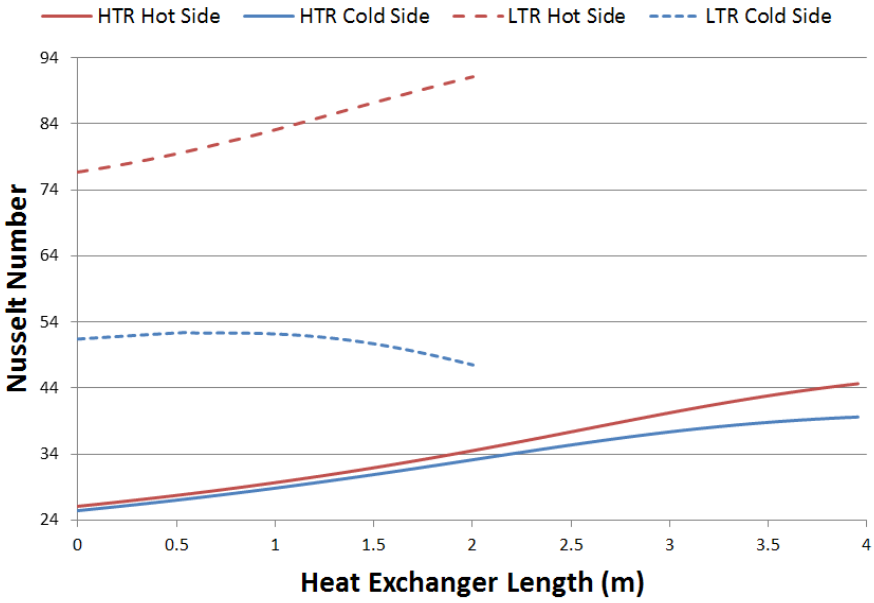

Figure 6-4: Fluid Nusselt number vs length of the recuperator

The Nusselt number curve in Figure 6-4 is largely affected by the trend in the Reynolds number. However, the two graphs do not match exactly, with the Nusselt number appearing to trend upward more. This is due to the Prandtl number also changing near the critical point.

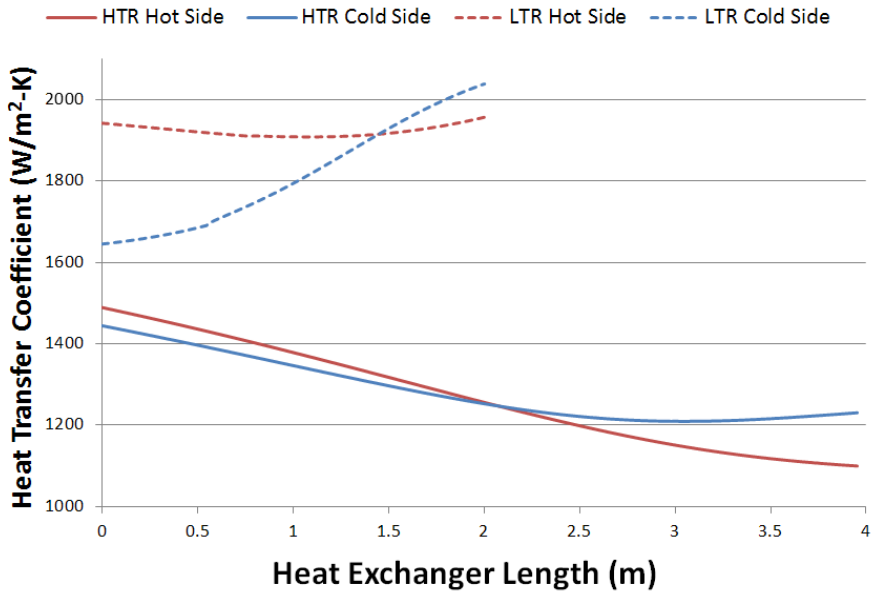

Figure 6-5: Fluid heat transfer coefficient vs length of the recuperator

The heat transfer coefficients, shown in Figure 6-5, follow an unusual behavior where the cold side crosses over the hot side in both the HTR and the LTR. Near the hotter end of the HTR, the heat transfer coefficient is highest due to thermal conductivity being highest. But the LTR experiences an increase in heat transfer coefficient due to SCO_2 property variation. Both recuperative heat exchangers experience a cross-over point where the cold side heat transfer coefficient becomes larger than the hot side heat transfer coefficient. This is due to the increasing influence of pressure the heat transfer coefficient as the fluid reaches critical temperature. Since the cold fluid is at a higher pressure, it will experience the greatest rise in conductivity and heat transfer coefficient. Future designs of heat exchangers may want to take advantage of this shift in heat transfer coefficient to minimize length and improve performance of the heat exchanger.

The linear temperature assumption is scrutinized for validity through a series of tests. The control volume number is increased, shortening the control volume length accordingly. The number of volumes is considered sufficient when the calculated outputs changed by less than 0.1%. Next, a fifth-order polynomial fit of the temperature profile is made using the least sum of squares method. The fit is very good for both the HTR and the LTR, having an r-squared of 1 and a maximum standard error of 0.08 K. The average temperature of the control volume is found using the linear approximation method and the polynomial curve fit. The difference between the two temperatures and the standard error are added together to find the maximum deviation in the linear estimate from the polynomial fit. In the HTR the linear assumption is accurate by a maximum of 0.024% and the LTR by 0.014%. Under this result 600 control volumes in the HTR and the 300 in the LTR are deemed sufficient.

6.2 High Temperature Recuperator Solid Modeling

The analytical model is brought into a solid model by contextualize a possible assembly method. One way the exchanger can be assembled by plates stacked on each other and fused together. The zigzag plates can be manufactured through additive, subtractive, or deformation methods. Using a solid model generated using Solidworks, a small scale example version of these heat exchangers is designed. The plates transition from a flat profile to a zigzag profile, seen on the left in Figure 6-6. The tips of these zigzag plates can be diffusion bonded to form the square channels. The flat plate portions will probably need a support structure, most likely guides that do not significantly disturb the flow. The counter flow heat exchanger can allow the flow to enter between every other plate. The flow then transitions into forming the square channels across their diagonal.

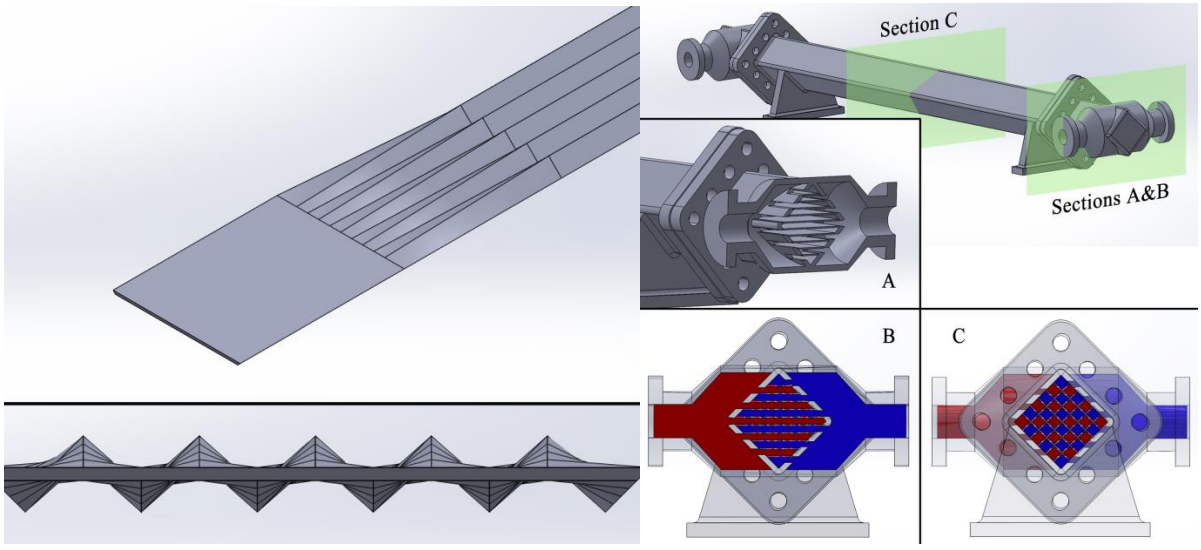

Figure 6-6: Example heat exchanger plate design, assembly, and manifold

The section views on the right side of Figure 6-6 demonstrate how these plates allow the flow to enter from the sides and transition through a manifold to the square pattern. This

transition will require further design considerations for stress and heat transfer. Modifications to the manifold design shown here can be made to allow the flow to more gently fill the channels. However, the transition from the flat plates to the square pattern should be made as quickly as possible to maximize heat transfer area in the square region.

7 DISCUSSION OF MODELING RESULTS

Now that multiple modeling methods are used to define the aerodynamics and heat transfer of SCO_2, the results are assessed. Recommendations are made to improve the robustness of the modeling methods.

7.1 Aerodynamics: One-Dimensional Mean-Line Compared to CFD

The behavior of the fluid as it passes through the turbo-expander first stage follows patterns laid out by the one-dimensional design. The variation of flow from hub to casing shows that the free vortex radial equilibrium condition correctly achieved in the model. The losses in the CFD model are similar to those of the one dimensional model.

Table 7-1: Deviation of CFD results from the one-dimensional model

	1-D	CFD	Difference
φ	0.529	0.523	-1.13%
α_2(º)	69.2	67.02	-3.15%
α_3(º)	6.9	4.21	-38.99%
β_2(º)	36.54	23.21	-36.48%
β_3(º)	63.55	59.34	-6.62%
C_1 (m/s)	96.74	95.58	-1.20%
C_2 (m/s)	272.18	253.3	-6.94%
C_3 (m/s)	97.45	107.3	10.11%
W_2 (m/s)	120.41	115.6	-3.99%
W_3 (m/s)	217.2	204.1	-6.03%
ζ_S	0.0687	0.0686	-0.15%
ζ_R	0.100	0.125	25.00%
η_{TS}(%)	82.9	82.2	-0.84%
η_{TT}(%)	90.5	90.4	-0.11%

Table 7-1 shows how the CFD deviates from the one-dimensional design specifications. The losses and efficiencies are calculated using the same equations as the one-dimensional method but with updated values from the CFD. Many of the flow parameters match within 10%. However, the relative flow angle at station two has a shallower angle than required for the design. This resulted in the incidence loss observed in Figure 5-13. In general, the flow velocities meet the initial design specifications.

$$\zeta_S \frac{1}{2}(C_2)^2 = h_2 - h_{2,isen} \quad \textbf{(7-1)}$$

$$\zeta_R \frac{1}{2}(W_3)^2 = h_3 - h_{3,isen} \quad \textbf{(7-2)}$$

Equations 7-1 and 7-2 show how the loss coefficients are calculated in Table 7-1. The theoretical, isentropic flow enthalpy is found and compared to the model enthalpy and flow velocity. The result is loss coefficients close to those predicted. When the CFD results are plugged into Equations 5-8 and 5-9, the projected efficiencies also match closely to the one-dimensional prediction. The enthalpy drop across the turbo-expander, according to CFD, is 42.2 kJ/kg. This corresponds to an 88% extraction of work from the total available enthalpy. That result is close to the efficiency predicted by the one-dimensional method.

7.2 Heat Transfer: Analytical Resistive Heat Exchange Model

The discretization approach provided interesting results describing the heat transfer capabilities of SCO_2. The code solved quickly and updated fluid properties directly from the REFPROP database without additional interpolation error. Interesting effects caused by variation in fluid properties are observed in the heat transfer coefficient.

One limitation of this method is that it relies on a repeating pattern of equally sized channels of heat exchange. This model can be sufficient in a recuperator where the same fluid is used for both flows. However, it is useful to be able to change the cross-sectional area of the channels for different fluids and different mass flows. This is achievable in a counter flow design, but the analytical method would need to be modified to account for the new walls of heat exchange and lateral conduction.

Another limitation of this method is its lack of automated optimization. For this study, finding the correct heat exchanger length is a system of guessing, converging on a solution, and updating the inputs until a desirable exchanger is sized. Automated optimization, like the methods proposed by Mohagheghi and Kapat (2013), would allow a map of available solutions for competing design objectives. Future work in this area should include experimental validation of the heat transfer model near and far from the critical point.

8 CONCLUSIONS

Carbon dioxide in its supercritical state presents a challenge for modeling. The physical properties of the fluid vary with temperature and pressure, especially near the critical point. A cycle energy balance optimization is performed to produce a SCO_2 power cycle with a competitive efficiency. An efficiency of 58.3% is feasible if the cycle components meet the required performance of the cycle calculations.

A one-dimensional mean-line approach is used to model the turbo-expander first stage. A basic loss model estimates that a 90% efficient is possible. The one-dimensional modeling method is brought into three dimensions and the stationary and the rotating airfoils are fully defined. The number of airfoils in the annular area is also designed so that the flow solid surrounding each airfoil can be attained.

The CFD model of the first turbo-expander stage demonstrates the capabilities of the design cascade to extract work from the fluid. According to the decrease in enthalpy, the stage is 90.4% efficient. This result agrees with the one-dimensional estimation of performance. Once the best design is determined, it should be validated experimentally.

The HTR and the LTR design requirements are successfully met by an analytical discretization modeling method. Sequentially arranged control volumes allow for fluid temperature, pressure and other properties to be modeled locally for the entire length of the heat exchanger. The HTR extracted 618.9 MW of energy and the LTR extracted 92.2 MW of energy from the hot fluid. The HTR and LTR are compact for their heat load, but require millions of millimeter-sized channels in order to meet the heat load required by the cycle.

A possible assembly of a compact heat exchanger is proposed for the HTR and the LTR at a commercial power plant. With diffusion bonding of large plates, the formation of this small channel exchanger is feasible. Future work should validate the models experimentally and define effective modifications to loss correlations in order to improve commercial SCO_2 power cycle design.

LIST OF REFERENCES

Ainley, D. G., & Mathieson, G. (1957). *A Method of Performance Estimation for Axial Flow Turbines.* R&M 2974. London: British Aeronautical Research Council.

Balje, O. E. (1981). *Turbomachines: A Guide to Design, Selection and Theory.* New York: Wiley and Sons, Inc.

Carman, B. G. (2002). *Design of a High Effectivenss Cermaic Micro-channel Heat Recuperator for Micro-turbine Application.* Orlando, Florida: University of Central Florida.

Chatharaju, M. (2011). *Computational Study of Critical Flow Discharge in Supercritical Water Cooled Reactors.* Hamilton, Ontario: McMaster University.

Dixon, S. L. (1975). *Fluid Mechanics, Thermodynamics of Turbomachinery* (2nd ed.). Oxford, United Kingdom: Pergamon Press.

Dostal, V. (2004). *A Supercritical Carbon Dioxide Cycle for Next Generation Nuclear Reactors.* Department of Nuclear Engineering. Boston, Massachusetts: Massachusetts Institute of Technology.

Fuller, R., Preuss, J., & Noall, J. (2012). Turbomachinery for Supercritical CO2 Power Cycles. *Proceedings of the ASME Turbo Expo.* Copenhagen, Denmark.

Horlock, J. H. (1966). *Axial Flow Turbines.* Oxford, United Kingdom: Butterworth and Co.

Jouybar, J., Eftari, M., Kaliji, H. D., Ghadak, F., & Rad, M. (2013). Analytical Modeling of Performance Characteristics of Axial Flow Two-Stage Turbine Engine Using Pressure Losses Models and Comparing with Experimental Results. *World Applied Sciences Journal, 9,* 1250-1259.

Kimball, K. J., & Clementoni, E. M. (2012). Supercritical Carbon Dioxide Brayton Power Cycle Development Overview. *Proceedings of the ASME Turbo Expo.* Copenhagen, Denmark.

Lemmon, E. W., Huber, M. L., & McLinden, M. O. (2013). NIST Standard Reference Database 23: Reference Fluid Thermodynamic and Transport Properties - REFPROP, Version 9.1. Gaithersburg, Maryland, United States of America.

Liao, S. M., & Zhao, T. S. (2002, June). Measurements of Heat Transfer Coefficients From Cupercritical Carbon Dioxide Flowing in Horizontal Mini/Micro Channels. *Journal of Heat Transfer, 124*, 413-420.

Mohagheghi, M., & Kapat, J. (2013). Thermodynamic Optimization of Recuperated S-CO2 Brayton Cycles for Solar Tower Applications. *Proceedings of the ASME Turbo Expo 2013.* San Antonio, Texas.

Pasch, J., Conboy, T., Fleming, D., & Rochau, G. (2012). *Supercritical CO2 Recompression Brayton Cycle: Completed Assembly Description.* Albuquerque, New Mexico: Sandia National Laboratories.

Persichilli, M., Kacludis, A., Zdankiewicz, E., & Held, T. (2012). Supercritical CO2 Power Cycle Developments and Commercialization: Why sCO2 can Displace Steam. *Proceedings of Power-Gen India & Central Asia.* New Delhi, India.

Soderberg, C. R. (1949). Unpublished Notes, Massachusetts Institute of Technology. *Fluid Mechanics and Thermodynamics of Turbomachinery*. Oxford, United Kingdom: Pergamon Press.

Southall, D. (2009). Diffusion Bonding in Compact Heat Exchangers. *Proceedings of SCO2 Power Cycle Symposium.* Troy, New York.

Turchi, C. S., Ma, Z., & Dyreby, J. (2012). Supercritical Carbon Dioxide Power Cycle Configurations for Use in Concentrating Solar Power Systems. *Proceedings of ASME Turbo Expo.* Copenhagen, Denmark.

Wang, K., Xu, X., Wu, Y., Liu, C., & Dang, C. (2014). Numerical Investigation on Heat Transfer of Supercritical CO2 in Heated Helically Coiled Tubes. *Journal of Supercritical Fluids*, 112-120.

Wei, N. (2000). *Significance of Loss Models in Aerothermodynamic Simulation for Axial Turbines.* Department of Energy Technology. Stockholm, Sweden: Royal Institute of Technology.

Wright, S. A., Radel, R. F., Vernon, M. E., Rochau, G. E., & Pickard, P. S. (2010). *Operation and Analysis of a Supercritical CO2 Brayton Cycle.* Advanced Nuclear Concepts Department. Albuquerque, New Mexico: Sandia National Laboratories.

Zhou, F. (2014). *Computational Fluid Dynamics Study of Convective Heat Transfer to Carbon Dioxide and Water at Supercritical Pressures in Vertical Circular Pipes.* Hamilton, Ontario: McMaster University.

Zweifel, O. (1946). Optimum Blade Pitch for Turbomachines with Special Reference to Blades of Great Curvature. *The Engineers' Digest, 7*, 358-360.